DYNAMICS AND TRAJECTORY OPTIMIZATION OF MORPHING AIRCRAFT IN PERCHING MANEUVERS

A Dissertation

Presented to the Faculty of the Graduate School

of Cornell University

In Partial Fulfillment of the Requirements for the Degree of

Doctor of Philosophy

by

Adam Michael Wickenheiser

January 2008

DYNAMICS AND TRAJECTORY OPTIMIZATION OF MORPHING AIRCRAFT IN PERCHING MANEUVERS

Adam Michael Wickenheiser, Ph. D.

Cornell University 2008

Advances in materials, actuators, and control architectures have enabled new design paradigms for unmanned aerial vehicles based on biological inspiration. Indeed, there has been a recent drive to design aircraft features and behaviors based on those of birds, insects, and flying mammals. This dissertation focuses on one such bio-inspired maneuver, perching, which can be described as a low-thrust, aerodynamically controlled, planted landing. While planted landings are possible in helicopters and jump jets, it has yet to be achieved on a low-thrust, high-efficiency platform such as a long loiter reconnaissance aircraft. It is proposed that in-flight shape reconfiguration can enable this class of aircraft to execute this maneuver without sacrificing its cruise performance.

This dissertation discusses the perching problem at various levels, from the aerodynamics of the wing to the complete trajectory of the maneuver. A lifting-line technique, a variant of Weissinger's classical method, is developed to analyze the aerodynamics of morphing wings in the attached flow regime. This tool is used both to study the effects of morphing on a wing's loading and to populate a database of aerodynamic coefficients for simulating the perching aircraft. Thusly, the aircraft is simulated in the longitudinal plane and compared to a similar fixed-configuration aircraft. Trim and stability analyses are performed on each aircraft in order to clarify

the effects of morphing on the aircraft's longitudinal dynamics. Finally, viable perching trajectories, which bring the aircraft from a cruise configuration to a planted landing, are developed and optimized in terms of their spatial requirements. Three classes of aircraft are simulated in this optimization study: point-mass, fixed-configuration (i.e. conventional), and morphing aircraft. Comparisons of these classes show that fixed-configuration aircraft are limited by their pitch maneuverability, whereas morphing can alleviate these limitations by increasing the available pitch authority. It is concluded that morphing increases pitch controllability during the maneuver while simultaneously decreasing the spatial requirements of the perching maneuver.

BIOGRAPHICAL SKETCH

Adam Wickenheiser received a Bachelor's of Science degree in Mechanical Engineering from Cornell University in 2002. He also qualified for a minor in Applied Mathematics. As an undergraduate, he was a researcher in the Cornell University Fluid Dynamics Laboratory and designed experiments for measuring vortex-induced vibrations on oscillating cylinders in moving fluids. He also participated in a NASA sponsored joint design project with Syracuse University to study structural and heat transfer properties of thermal tiles for a next-generation reentry vehicle. He attained an overall GPA of 4.2, the second highest in his graduating class.

Upon graduating, Adam continued into the doctoral program at Cornell University, receiving a prestigious Cornell Graduate Research Fellowship for his first year of graduate study. He joined the Laboratory for Intelligent Machine Systems, directed by Prof. Ephrahim Garcia, in 2003. During the same year, he was admitted into the Graduate Student Research Program at NASA Langley Research Center, receiving a three-year fellowship for work on morphing aircraft dynamics and control. As part of this program, he worked at NASA Langley during the summers of 2003-2005 in the Dynamics & Controls Branch, under the advisement of Mr. Martin Waszak. In January 2006, he received a Master's of Science degree in Aerospace Engineering for his research entitled "Dynamics and Control of Morphing Aircraft in Perching Maneuvers".

Subsequently, Adam continued his research on perching aircraft at Cornell University. In 2006, he received an ASEE Air Force Summer Graduate Student Award from Wright-Patterson AFB to conduct research on base during the summer. This work

included the development of a finite-element structural code combined with a panel-method aerodynamic code for use in modeling morphing wing dynamics. During his doctoral studies, Adam published two papers in the Journal of Aircraft and submitted one paper to the Journal of Guidance, Control, and Dynamics for review.

ACKNOWLEDGMENTS

I want to thank my parents for their years of support, for smiling and nodding whenever I tried to explain my research to them, and for reminding me that I can't stay a student forever, despite my best efforts. My lab mates Tim Reissman, Justin Manzo, and John Dietl for their great advice, for their terrible jokes, and for putting up with me those times I seemed to lose my mind from overexposure to Matlab. The Big Red Barn for providing a weekly reminder that grad school can be highly amusing at times. Cornell University, NASA Langley, Wright-Patterson AFB, and the DSO for funding my research and supporting me during grad school. Dan Sunshine, Carl Whittaker, Jason Harris, Wen Rong Lim, and Joe Andrews for their great help in developing experiments and hardware for my project. Prof. David Caughey and Prof. Jane Wang for their help in preparing for my exams and this dissertation. Finally, I'd like to thank my advisor, Prof. Ephrahim Garcia, for his great words of wisdom – academic, professional, and otherwise – and for inspiring me always to earn my take-home pay.

TABLE OF CONTENTS

LIST OF FIGURES

LIST OF TABLES

LIST OF ABBREVIATIONS

ARES	Aerial Regional-Scale Environmental Survey
ARES-C	Aerial Regional-Scale Environmental Survey (at Cornell)
c.g.	Center of Gravity
c.p.	Center of Pressure
CFD	Computational Fluid Dynamics
Datcom	Data Compendium
ISR	Intelligence, Surveillance, and Reconnaissance
UAV	Unmanned Aerial Vehicle
USAF	United States Air Force
V/STOL	Vertical/Short Take-Off and Landing

LIST OF SYMBOLS

CHAPTER 1

a	wing curvature parameter
b	wing span
c	local chord length
$\hat{c}$	local nondimensional chord length
$\bar{c}$	mean aerodynamic chord
$\hat{\bar{c}}$	nondimensional mean aerodynamic chord
C_l	section lift coefficient
C_d	section drag coefficient
C_L	wing lift force coefficient
C_D	wing drag force coefficient
C_Y	wing side force coefficient
C_L	wing roll moment coefficient
C_M	wing pitch moment coefficient
C_N	wing yaw moment coefficient
C_{l_α}	section lift curve slope
G	nondimensional circulation
L	wing lift force
l	section lift force/length
m	number of points used in sine series expansion of circulation function
M	number of points used in trapezoidal approximation
Q	dynamic pressure
$\mathbf{r}$	displacement vector
S	wing planform area

$\hat{S}$	nondimensional wing planform area
U_∞	free stream velocity magnitude
$\mathbf{v}$	wind velocity vector
w	downwash velocity
x_{cp}	position of the wing center of pressure
x_{cg}	position of the wing center of gravity
$x_{c/4}$	position of the airfoil quarter-chord point
y_0	wing semi-span, y-coordinate of wingtip
α	wind incidence angle/angle of attack
α_{0L}	angle of attack for zero lift
Λ	wing aspect ratio
ε	downwash angle at wing ¼-chord line
Γ	circulation magnitude
$\boldsymbol{\Gamma}$	vorticity vector
η	nondimensional spanwise coordinate
ξ	nondimensional chordwise coordinate
σ	planar density
$\mathcal{L}$	wing roll moment
$\mathcal{M}$	wing pitch moment
$\mathcal{N}$	wing yaw moment

CHAPTER 2

D	aircraft drag force
f_x, X	x-component of external force
f_z, Z	z-component of external force
$\mathbf{f}$	external force vector

g	gravity magnitude
$\mathbf{g}$	gravity vector
I_y	principal moment of inertia about y-axis
$\mathbf{I}$	moment of inertia matrix
L	aircraft lift force
M	aircraft pitch moment
m	aircraft mass
m_y	y-component of external moment
$\mathbf{m}$	external moment vector
q	pitch rate
$\mathbf{q}$	quaternion
T	thrust magnitude
$\mathbf{T}$	transformation matrix from body- to earth-coordinates
u	x-component of aircraft velocity
V	aircraft velocity magnitude
v	y-component of aircraft velocity
$\mathbf{v}$	aircraft velocity vector (body coordinates)
w	z-component of aircraft velocity
x	forward direction
$\mathbf{x}$	aircraft position vector (inertial coordinates)
y	sidereal direction
z	vertical direction
α	angle of attack
β	sideslip angle
δ_a	aileron deflection angle
δ_e	elevator or symmetric ruddervator deflection angle

θ	pitch angle
θ_b	boom angle with respect to fuselage
θ_t	tail angle with respect to boom
Θ_0	trim pitch angle
$\imath$	wing incidence angle
ϕ	roll angle
ψ	yaw angle
$\boldsymbol{\omega}$	aircraft angular velocity vector
$\boldsymbol{\omega}^{\times}$	skew-symmetric cross product matrix of $\boldsymbol{\omega}$

CHAPTER 3

C_D	drag coefficient
C_L	lift coefficient
C_M	pitch moment coefficient
C_{M_q}	pitch damping coefficient
c	local chord length
$\bar{c}$	mean aerodynamic chord
g	acceleration due to gravity
h	vertical position
I_y	principal moment of inertia about pitch axis
J	cost function
l	characteristic length
m	aircraft mass
p	dynamic mixing parameter
p_0	static mixing parameter
q	pitch rate

S	planform area
T	thrust magnitude
T/W	thrust-to-weight ratio
t	time
V	aircraft velocity magnitude
x	horizontal position
x_{cg}	aircraft center of gravity
x_{cp}	airfoil center of pressure
x_{np}	aircraft neutral point
$\mathbf{x}$	state vector
α	angle of attack
γ	flight path angle
δ_e	elevator deflection angle
θ	pitch angle
θ_b	tail boom angle with respect to fuselage
θ_t	tail angle with respect to boom
$\imath$	wing incidence angle with respect to fuselage
κ	pitch moment scaling factor
ρ	air density
τ_1, τ_2	time constants

Subscripts

0	initial
f	final
att	attached flow regime
climb	climb phase

dive	dive phase
fuse	fuselage lifting surface
sep	separated flow regime
tail	tail lifting surface
wing	wing lifting surfaces

CHAPTER 1
AERODYNAMIC MODELING OF MORPHING WINGS USING AN EXTENDED LIFTING-LINE ANALYSIS[1]

1. Abstract

This chapter presents an extension of Weissinger's method and its use in analyzing morphing wings. This method is shown to be ideal for preliminary analyses of these wings due to its speed and adaptability to many disparate wing geometries. It extends Prandtl's lifting-line theory to planform wings of arbitrary curvature and chord distribution and non-ideal airfoil cross sections. The problem formulation described herein leads to an integrodifferential equation for the unknown circulation distribution. It is solved using Gaussian quadrature and a sine-series representation of this distribution. In this chapter, this technique is used to analyze the aerodynamics of a morphable gull-like wing. Specifically, this wing's ability to manipulate lift-to-drag efficiency and center of pressure location is discussed.

2. Introduction

Throughout the history of aviation, very little of man's inspiration for flight has manifested itself in aircraft designs. Indeed, manmade flight bears little resemblance to avian morphologies, which are backed by millions of years of evolution. Birds morph their wings and tail in complex, fluid ways, in contrast to the limited range of motion of an aircraft's control surfaces. Most aircraft deploy flaps and slats during takeoff and landing in order to increase lift at slower speeds. This is an example of a

[1] From Wickenheiser, A. and Garcia, E., "Aerodynamic Modeling of Morphing Wings Using an Extended Lifting-Line Analysis"; reprinted by permission of the American Institute of Aeronautics and Astronautics, Inc.

configuration change that occurs continuously during avian flight. A bird's morphology allows it to constantly change its wing and tail shapes to suit flight at a wide range of speeds.

Recently, research and development have begun on a new concept that challenges current designs: morphing aircraft [1]. A morphing aircraft is an aircraft capable of controlled, gross shape changes in-flight, with the purpose of increasing efficiency, versatility, and/or mission performance. While traditional aircraft are designed as compromises of various performance needs, a single morphing aircraft can excel at numerous tasks [2,3]. The same airframe can morph from a highly efficient glider to a fast, high maneuverability vehicle. While a traditional wing is designed for high efficiency over a small range of flight conditions, a morphing wing can adapt to grossly different altitudes and flight speeds. Morphing technologies enable new flight capabilities, such as perching, urban navigation, and indoor flight. These capabilities have heretofore been unrealizable due to technological limitations. Modern development of smart structures, adaptive materials, and distributed and adaptive control theory has opened the door to a host of new aircraft designs and flight capabilities [4].

These new capabilities are realized by the careful manipulation of aerodynamic forces and moments. For example, a long endurance aircraft benefits from a high lift-to-drag ratio, while a highly maneuverable aircraft needs high lift and low (or negative) stability margins. Highly efficient cruise can be accomplished by morphing the wing cross sections to maintain high lift-to-drag ratios at various flight speeds and altitudes. New capabilities, such as perching, can be achieved by controlling the degree of separated flow over the aircraft's lifting surfaces [5]. Many of these capabilities

require levels of actuation far exceeding the bounds of conventional aircraft control surfaces.

Unlike most traditional aircraft, morphing aircraft concepts require an aerodynamic analysis for both varying flight conditions and grossly varying geometric configurations. This requirement demands a preliminary analysis methodology that is fast, accurate, and reconfigurable, without having to rebuild the mesh of the aircraft or flow field, for example. Consequently, a lifting-line approach is chosen over a computational fluid dynamics (CFD) approach as the aerodynamic modeling method. This method effectively breaks the 3-D wing into a series of 2-D airfoils joined by their quarter-chord curve, as depicted in Figure 1.1.

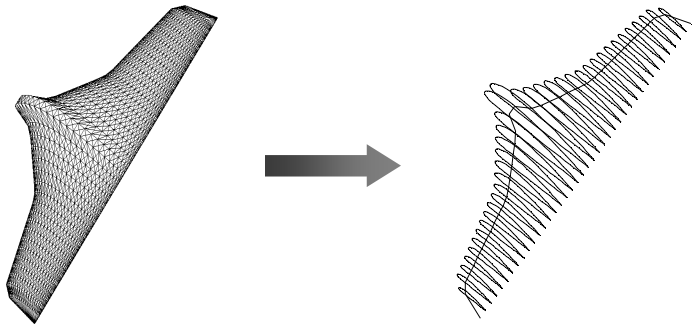

Figure 1.1: Lifting line theory effectively decouples the 3-D panel problem into a series of 2-D airfoils

The analytic nature of this method allows the wing geometries to be programmed as functions into generic software environments such as Matlab or C. Consequently, changing geometry parameters, such as the wing curvature parameter presented below, may be placed in a software loop in order to automatically generate many wing geometry variations.

Weissinger's method for straight, swept wings is the basis of the present lifting-line theory [6]. His method relates the downwash air velocity at any given span station on the wing to the sum of the downwash contributions of the vortex line attached to the quarter-chord line of the wing and the semi-infinite vortex sheet trailing behind it. This method does not consider the geometry of the wing cross sections or the non-planarity of the wake. An effort is made, as explained below, to account for the former by introducing real airfoil data for each of the span stations. Although full 3-D analysis tools such as panel methods and CFD software do not require a separate database of airfoil data in this event, computationally it is more efficient to have these data tabulated beforehand. The method presented below only has to reference these data instead of needing to re-compute them in its algorithm. This method has been extended to curved wings of a specific (polynomial) form by Prössdorf and Tordella [7] for stationary wings and by Chiocchia, et al. [8] for wings in oscillatory motion. The problem formulation leads to an integrodifferential equation as shown in the next section. This equation is solved assuming a sine series representation of the circulation, which conforms to the boundary conditions of no circulation at the wingtips. Gaussian quadrature and the trapezoidal rule are then used to compute the integrals. This technique results in a relatively high $1/M^2$ error, where M is the number of function evaluations; however, this number may be increased independently from the number of span stations m used in the aerodynamic calculations, as shown below. Prössdorf shows that error in the calculated circulation distribution decreases exponentially with m, assuming that the quarter-chord curve can be bounded by a polynomial [7].

This analysis is shown to be effective in computing the lift and drag distributions over a variety of wing geometries. Although this method assumes no separation effects, it

is valid in the Reynolds number regime of medium-scale UAVs and larger aircraft at moderate angles of attack, where viscous effects are minimal. This method's speed and reconfigurability make it ideal for the preliminary analysis of morphing wings with a large number of varying geometrical parameters. This method is also useful in the construction of an aerodynamic lookup table for use in an aircraft simulation, for example.

3. Problem Formulation

A model of the wing geometry and the flow field is developed in order to formulate the circulation distribution along the span. The circulation is found by examining the downwash velocity distribution in the wake of the lifting surface. First, a Cartesian coordinate system is established such that the positive x-direction points downstream, parallel to the free-stream velocity U_∞, and the positive y-direction points towards the right wingtip. (Thus, by the right-hand rule, the positive z-direction points outward from the page.) The quarter chord of the wing is represented by a continuous, piecewise differentiable function that extends from $y = -y_0$ to $y = y_0$, not necessarily symmetric about the x-axis but contained entirely in the xy-plane. The chord and twist distributions are given as piecewise continuous functions of the spanwise coordinate. The model of the flow field consists of a bound or lifting vortex at the quarter chord curve of the wing and a trailing vortex sheet that extends to infinity downstream. The downwash at each point in the flow field is therefore the sum of the velocities induced by the lifting vortex and the distributed vortex sheet. These two contributions are shown in Figure 1.2, where the geometry is defined in a similar manner to Prössdorf [7] and DeYoung [9]. Since the flow field is modeled as a superposition of potential flows, this method only applies when viscous effects are not significant.

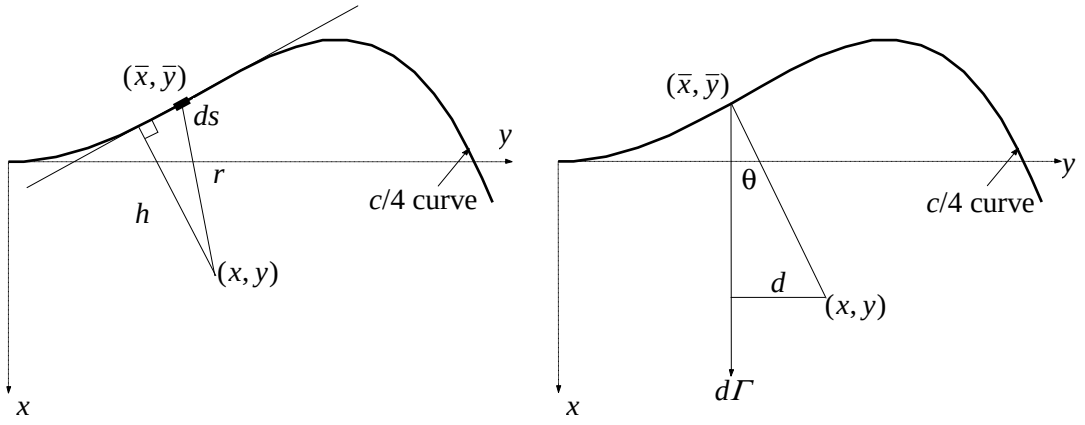

Figure 1.2: Schematic of the downwash contribution by a segment *ds* of the lifting vortex (a). Schematic of the downwash contribution by a vortex filament *d*Γ of the trailing vortex system (b).

The contributions of the lifting and trailing vortices to the downwash velocity *w* can be calculated by the Biot-Savart Law:

$$\mathbf{v} = \frac{1}{4\pi}\int \frac{\boldsymbol{\Gamma}\times\mathbf{r}}{|\mathbf{r}|^3} ds\,, \tag{1}$$

which gives the fluid velocity at any point displaced from a vortex element of strength Γ. Using this law, the downwash caused by segment *ds* of the lifting vortex is given by

$$dw(x,y) = \frac{\Gamma h ds}{4\pi r^3}\,. \tag{2}$$

where the geometry is defined in Figure 1.2(a). In terms of the points (x,y) in the plane of the wing and $(\bar{x},\bar{y})$ along the quarter-chord curve, Eq. (2) becomes

$$dw(x,y) = \Gamma(\bar{y})\frac{[x-\bar{x}(\bar{y})+\bar{x}'(\bar{y})(\bar{y}-y)]d\bar{y}}{4\pi\left[(x-\bar{x}(\bar{y}))^2+(y-\bar{y})^2\right]^{3/2}}\,, \tag{3}$$

where

$$\bar{x}'(\bar{y}) = \left.\frac{d\bar{x}(y)}{dy}\right|_{y=\bar{y}} .$$

The downwash caused by an infinitesimal vortex filament $d\Gamma$ in the trailing vortex sheet is given by

$$dw(x,y) = \frac{d\Gamma}{4\pi d}(\cos\theta + 1) \tag{4}$$

where the geometry is defined in Figure 1.2(b). In terms of the points (x, y) and $(\bar{x}, \bar{y})$, Eq. (4) becomes

$$dw(x,y) = \frac{\Gamma'(\bar{y})}{4\pi(y-\bar{y})}\left(\frac{x-\bar{x}(\bar{y})}{\sqrt{(x-\bar{x}(\bar{y}))^2 + (y-\bar{y})^2}} + 1\right) d\bar{y} , \tag{5}$$

where

$$\Gamma'(\bar{y}) = \left.\frac{d\Gamma(y)}{dy}\right|_{y=\bar{y}} .$$

Summing Eqs. (3) and (5) and integrating from $-y_0$ to y_0 gives the total downwash at the point (x, y) in the flow field:

$$\begin{aligned} w(x,y) = {} & \frac{1}{4\pi}\int_{-y_0}^{y_0} \frac{\Gamma'(\bar{y})}{y-\bar{y}}\, d\bar{y} \\ & + \frac{1}{4\pi}\int_{-y_0}^{y_0} \frac{\Gamma'(\bar{y})}{y-\bar{y}} \frac{x-\bar{x}(\bar{y})}{\sqrt{(x-\bar{x}(\bar{y}))^2 + (y-\bar{y})^2}}\, d\bar{y} \\ & + \frac{1}{4\pi}\int_{-y_0}^{y_0} \Gamma(\bar{y}) \frac{x-\bar{x}(\bar{y}) + \bar{x}'(\bar{y})(\bar{y}-y)}{\left[(x-\bar{x}(\bar{y}))^2 + (y-\bar{y})^2\right]^{3/2}}\, d\bar{y} \end{aligned} \tag{6}$$

The first two integrals in Eq. (6) have singularities at $\bar{y} = y$; however, only the second integral diverges near the singularity. (The singularity in the first integral will be

addressed below.) To remove this discontinuity, the first term is added to and subtracted from Eq. (6), as recommended by DeYoung [9], resulting in

$$\begin{aligned} w(x,y) = & \frac{1}{2\pi}\int_{-y_0}^{y_0}\frac{\Gamma'(\bar{y})}{y-\bar{y}}d\bar{y} \\ & + \frac{1}{4\pi}\int_{-y_0}^{y_0}\frac{\Gamma'(\bar{y})}{y-\bar{y}}\left[\frac{x-\bar{x}(\bar{y})}{\sqrt{(x-\bar{x}(\bar{y}))^2+(y-\bar{y})^2}}-1\right]d\bar{y} \\ & + \frac{1}{4\pi}\int_{-y_0}^{y_0}\Gamma(\bar{y})\frac{x-\bar{x}(\bar{y})+\bar{x}'(\bar{y})(\bar{y}-y)}{\left[(x-\bar{x}(\bar{y}))^2+(y-\bar{y})^2\right]^{3/2}}d\bar{y} \end{aligned} \tag{7}$$

which is referred to as the dimensional form of the modified Weissinger's method. According to the Pistolesi-Weissinger condition [6,10], the overall wind velocity should be tangent to the plane of the wing at the wing's ¾-chord line. In other words, along this line the downwash angle is equal to the local airfoil's angle of attack, which is the sum of the wing's geometrical twist and its overall angle of attack. Thus, the downwash velocity *w* in Eq. (7) should be evaluated at

$$x = \bar{x}(y) + \frac{c(y)}{2}, \tag{8}$$

which is half a chord length behind the quarter-chord line. With this substitution, Eq. (7) becomes

$$\begin{aligned} w(y) = & \frac{1}{2\pi}\int_{-y_0}^{y_0}\frac{\Gamma'(\bar{y})}{y-\bar{y}}d\bar{y} \\ & + \frac{1}{4\pi}\int_{-y_0}^{y_0}\frac{\Gamma'(\bar{y})}{y-\bar{y}}\left[\frac{\bar{x}(y)-\bar{x}(\bar{y})+c(y)/2}{\sqrt{(\bar{x}(y)-\bar{x}(\bar{y})+c(y)/2)^2+(y-\bar{y})^2}}-1\right]d\bar{y}, \\ & + \frac{1}{4\pi}\int_{-y_0}^{y_0}\Gamma(\bar{y})\frac{\bar{x}(y)-\bar{x}(\bar{y})+c(y)/2+\bar{x}'(\bar{y})(\bar{y}-y)}{\left[(\bar{x}(y)-\bar{x}(\bar{y})+c(y)/2)^2+(y-\bar{y})^2\right]^{3/2}}d\bar{y} \end{aligned} \tag{9}$$

where the downwash is now only a function of the spanwise coordinate. If the geometry for a straight, swept wing is substituted into Eq. (9), then the lifting-line formula derived by Weissinger [6] and DeYoung [9] can be recovered.

4. Solution Procedure

Equation (9) gives the downwash caused by the lifting vortex and the trailing vortex sheet at the point *y* along the ¾-chord line; this downwash should be equal to the upwash felt by the wing due to its local incidence to the flow. Therefore, the only unknown quantity in Eq. (9) is the circulation distribution $\Gamma(y)$. Although $\Gamma(y)$ has no explicit solution, it can be approximated to an arbitrary accuracy by a sine series, as first shown by Multhopp [11]. A transformation to trigonometric coordinates will then allow the exact integration of the first term in Eq. (9) and a simplification of the other two terms. The trapezoidal method is then used to integrate the second and third terms. As will be shown, the number of terms used in this integration can be made independent of the number of terms used in the sine series representation of $\Gamma(y)$.
It is now convenient to convert Eq. (9) to non-dimensional form by introducing the following dimensionless variables:

$$\eta = \frac{y}{y_0}\ , \qquad \overline{\eta} = \frac{\bar{y}}{y_0}, \qquad G = \frac{\Gamma}{y_0 U_\infty},$$

$$\overline{\xi} = \frac{\bar{x}}{c}, \qquad \alpha = \frac{w}{U_\infty}. \tag{10}$$

Here, it is assumed that all downwash angles are small. In dimensionless form, Eq. (9) can now be written as

$$\alpha(\eta) = \frac{1}{2\pi}\int_{-1}^{1}\frac{G'(\bar{\eta})}{\eta-\bar{\eta}}d\bar{\eta} + \frac{1}{4\pi}\int_{-1}^{1}\frac{G'(\bar{\eta})}{\eta-\bar{\eta}}\left[\frac{\bar{\xi}(\eta)-\bar{\xi}(\bar{\eta})+1/2}{\sqrt{\left(\bar{\xi}(\eta)-\bar{\xi}(\bar{\eta})+1/2\right)^2+\left(y_0/c(\eta)\right)^2(\eta-\bar{\eta})^2}}-1\right]d\bar{\eta} + \frac{1}{4\pi}\left(\frac{y_0}{c(\eta)}\right)^2\int_{-1}^{1}G(\bar{\eta})\frac{\bar{\xi}(\eta)-\bar{\xi}(\bar{\eta})+1/2+\bar{\xi}'(\bar{\eta})(\bar{\eta}-\eta)}{\left[\left(\bar{\xi}(\eta)-\bar{\xi}(\bar{\eta})+1/2\right)^2+\left(y_0/c(\eta)\right)^2(\eta-\bar{\eta})^2\right]^{3/2}}d\bar{\eta} \tag{11}$$

In order to simplify the integrals in Eq. (11) and cast $G(\bar{\eta})$ as a sine series, the spanwise coordinates are transformed into angles by the following definitions:

$$\phi_v \equiv \cos^{-1}(\eta) \text{ and } \phi \equiv \cos^{-1}(\bar{\eta}). \tag{12}$$

For simplicity, let

$$P(\eta,\bar{\eta}) \equiv \frac{1}{\eta-\bar{\eta}}\left[\frac{\bar{\xi}(\eta)-\bar{\xi}(\bar{\eta})+1/2}{\sqrt{\left(\bar{\xi}(\eta)-\bar{\xi}(\bar{\eta})+1/2\right)^2+\left(y_0/c(\eta)\right)^2(\eta-\bar{\eta})^2}}-1\right]$$
$$R(\eta,\bar{\eta}) \equiv \frac{\bar{\xi}(\eta)-\bar{\xi}(\bar{\eta})+1/2+\bar{\xi}'(\bar{\eta})(\bar{\eta}-\eta)}{\left[\left(\bar{\xi}(\eta)-\bar{\xi}(\bar{\eta})+1/2\right)^2+\left(y_0/c(\eta)\right)^2(\eta-\bar{\eta})^2\right]^{3/2}} \tag{13}$$

After these substitutions, Eq. (11) becomes

$$\alpha(\phi_v) = \frac{1}{2\pi}\int_0^{\pi}\frac{G'(\phi)}{\cos\phi-\cos\phi_v}d\phi - \frac{1}{4\pi}\int_0^{\pi}P(\phi_v,\phi)G'(\phi)d\phi + \frac{1}{4\pi}\left(\frac{y_0}{c(\phi_v)}\right)^2\int_0^{\pi}R(\phi_v,\phi)G(\phi)\sin\phi d\phi \tag{14}$$

.

In order to solve Eq. (14) for the unknown function $G(\phi)$, it is assumed that $G(\phi)$ can be represented as a sine series of m terms. (Note that this representation meets the boundary conditions of no circulation at the wingtips, that is $G(0) = G(\pi) = 0$.) Let

$$G(\phi) = \sum_{k=1}^{m} a_k \sin(k\phi), \text{ where } a_k = \frac{2}{\pi}\int_0^{\pi}G(\phi)\sin(k\phi)d\phi. \tag{15}$$

Multhopp's formula [11], based on Gaussian quadrature, is used to evaluate the integral in Eq. (15). This method will exactly integrate a sequence of orthogonal functions such as the sine series representation of $G(\phi)$ if m points are chosen for the quadrature. These points must be located at the roots of the next function in the sequence, $\sin[(m+1)\pi]$. Applying this quadrature to Eq. (15) yields

$$a_k = \frac{2}{m+1}\sum_{n=1}^{m} G(\phi_n)\sin(k\phi_n), \text{ where } \phi_n = \frac{n\pi}{m+1}, \tag{16}$$

where the ϕ_n are the roots of the next function in the sine series. Therefore,

$$G(\phi) = \frac{2}{m+1}\sum_{n=1}^{m} G(\phi_n)\sum_{k=1}^{m} \sin(k\phi_n)\sin(k\phi)$$

$$G'(\phi) = \frac{2}{m+1}\sum_{n=1}^{m} G(\phi_n)\sum_{k=1}^{m} k\sin(k\phi_n)\cos(k\phi). \tag{17}$$

With the definitions

$$f_n(\phi) \equiv \frac{2}{m+1}\sum_{k=1}^{m} \sin(k\phi_n)\sin(k\phi)$$

$$h_n(\phi) \equiv \frac{2}{m+1}\sum_{k=1}^{m} k\sin(k\phi_n)\cos(k\phi)$$

$$G_n \equiv G(\phi_n), \tag{18}$$

Eq. (17) can be written as

$$G(\phi) = \sum_{n=1}^{m} G_n f_n(\phi) \text{ and } G'(\phi) = \sum_{n=1}^{m} G_n h_n(\phi). \tag{19}$$

Substituting Eqs.(18) and (19) into Eq. (14) gives

$$\alpha(\phi_v) = \frac{1}{\pi(m+1)} \sum_{n=1}^{m} G_n \sum_{k=1}^{m} k \sin(k\phi_n) \int_0^{\pi} \frac{\cos(k\phi)}{\cos\phi - \cos\phi_v} d\phi$$
$$- \frac{1}{4\pi} \sum_{n=1}^{m} G_n \int_0^{\pi} P(\phi_v, \phi) h_n(\phi) d\phi \qquad . \qquad (20)$$
$$+ \frac{1}{4\pi} \left(\frac{y_0}{c(\phi_v)} \right)^2 \sum_{n=1}^{m} G_n \int_0^{\pi} R(\phi_v, \phi) f_n(\phi) \sin\phi d\phi$$

Although the first integral has a singularity at $\phi = \phi_v$, the integral is finite and given by the formula

$$\int_0^{\pi} \frac{\cos(k\phi)}{\cos\phi - \cos\phi_v} d\phi = \frac{\pi \sin(k\phi_v)}{\sin\phi_v}, \qquad (21)$$

derived by Glauert [12]. The trapezoidal method is used to evaluate the second and third integrals in Eq. (20). This formula is given by

$$\int_0^{\pi} F(\phi) d\phi \approx \frac{\pi}{M+1} \left[\frac{F(0) + F(\pi)}{2} + \sum_{\mu=1}^{M} F(\phi_\mu) \right] \qquad (22)$$

where

$$\phi_\mu = \frac{\mu\pi}{M+1},$$

for a general function $F(\phi)$. The integer M dictates how many function evaluations are used to compute the integral and is independent of m, the number of terms in the sine series representation of $G(\phi)$. Using Eqs. (21) and (22) to evaluate the integrals in Eq. (20) gives

$$\alpha(\phi_v) = \frac{1}{m+1} \sum_{n=1}^{m} G_n \sum_{k=1}^{m} \frac{k \sin(k\phi_n) \sin(k\phi_v)}{\sin\varphi_v}$$
$$- \frac{1}{4(M+1)} \sum_{n=1}^{m} G_n \left[\frac{P(\phi_v, 0) h_n(0) + P(\phi_v, \pi) h_n(\pi)}{2} + \sum_{\mu=1}^{M} P(\phi_v, \phi_\mu) h_n(\phi_\mu) \right] . \qquad (23)$$
$$+ \frac{1}{4(M+1)} \left(\frac{y_0}{c(\phi_v)} \right)^2 \sum_{n=1}^{m} G_n \sum_{\mu=1}^{M} R(\phi_v, \phi_\mu) f_n(\phi_\mu) \sin\phi_\mu$$

The sum in the first term of Eq. (23) has an explicit formula, given by

$$\frac{1}{m+1}\sum_{k=1}^{m}\frac{k\sin(k\phi_n)\sin(k\phi_v)}{\sin\phi_v}=\begin{cases}\dfrac{m+1}{4\sin\phi_v}, & n=v\\ \dfrac{-\sin\phi_n}{(\cos\phi_n-\cos\phi_v)^2}, & n\neq v\end{cases} \tag{24}$$

Equation (23) relates the airfoil angle of attack at ϕ_v to a linear combination of circulation function evaluations G_n. Since $\alpha(\phi)$ is a known function, it can be evaluated at m distinct points to create a system of equations for G_n. Constructing the matrix

$$\begin{aligned}\mathbf{A}=&\frac{1}{m+1}\sum_{k=1}^{m}\frac{k\sin(k\phi_n)\sin(k\phi_v)}{\sin\phi_v}\\ &-\frac{1}{4(M+1)}\left[\frac{P(\phi_v,0)h_n(0)+P(\phi_v,\pi)h_n(\pi)}{2}+\sum_{\mu=1}^{M}P(\phi_v,\phi_\mu)h_n(\phi_\mu)\right],\\ &+\frac{1}{4(M+1)}\left(\frac{y_0}{c(\phi_v)}\right)^2\sum_{\mu=1}^{M}R(\phi_v,\phi_\mu)f_n(\phi_\mu)\sin\phi_\mu\end{aligned} \tag{25}$$

where the *vn*-th component is evaluated at ϕ_v and ϕ_n, Eq. (23) becomes

$$\vec{\boldsymbol{\alpha}}=\mathbf{A}\vec{\mathbf{G}}\text{, where }\vec{\boldsymbol{\alpha}}=\begin{bmatrix}\alpha(\phi_1)\\ \vdots\\ \alpha(\phi_m)\end{bmatrix}\text{ and }\vec{\mathbf{G}}=\begin{bmatrix}G_1\\ \vdots\\ G_m\end{bmatrix}. \tag{26}$$

This is a system of *m* equations for the unknowns G_n. The vector $\vec{\boldsymbol{\alpha}}$ is comprised of the local angle of attack values at $\phi_1, \ldots, \phi_m$, and $\vec{\mathbf{G}}$ is a vector of unknowns. The G_n can be computed by inverting **A**, and the circulation distribution can be reconstructed using Eq. (19).

So far, this analysis has assumed that the airfoil cross sections of the wing are ideal; that is, they have a lift curve slope of 2π and generate no lift at a zero-degree angle of

attack. It is desired to incorporate real airfoil data into this lifting-line analysis in order to predict better the lift on real aircraft wings. This incorporation will also help evaluate the effects of airfoil morphing on the entire wing's aerodynamic properties. These data may be obtained from experiment or computation; however, as stated previously, they are only referenced by this algorithm and not recomputed. In order to assimilate non-ideal airfoils, DeYoung suggests the method of distorting the chord length distribution along the wing such that the dimensional circulation about every span station matches the dimensional circulation of an ideal airfoil with the original chord length [9]. Alternatively, this can be accomplished by offsetting the left-hand side of Eq. (23) by the true angle of attack for zero lift of that section and scaling it by the ratio of its lift curve slope to that of an ideal airfoil. Consequently, the left-hand side becomes

$$\frac{C_{l_\alpha}(\phi_v)}{2\pi}\left[\alpha(\phi_v)-\alpha_{0L}(\phi_v)\right]=\cdots. \tag{27}$$

The downwash angle at each wing station can now be computed. By Munk's analysis [13], the downwash angle is given by half the downwash angle an infinite distance downstream. To calculate this, take half the limit of Eq. (7) as x goes to infinity:

$$\frac{1}{2}\lim_{x\to\infty} w(x,y)=\frac{1}{4\pi}\int_{-y_0}^{y_0}\frac{\Gamma'(\bar{y})}{y-\bar{y}}\,d\bar{y}\,. \tag{28}$$

By converting Eq. (28) to non-dimensional form and casting it terms of the sine series coefficients, the downwash angle ε at station ϕ_v is given by

$$\varepsilon(\phi_v)=\frac{1}{2(m+1)}\sum_{n=1}^{m}G_n\sum_{k=1}^{m}\frac{k\sin(k\phi_n)\sin(k\phi_v)}{\sin\phi_v}, \tag{29}$$

which is one half the first term in Eq. (23). With the downwash angle given by Eq. (29), the overall wind incidence angle (wing angle of attack + wing twist + downwash

angle) can be computed at each station. Although this angle is computed using potential theory, it can be used to acquire a good approximation of section lift and drag forces if real airfoil data are available. The overall wind incidence angle is used in lieu of the angle of attack in determining section lift (C_l) and drag (C_d) coefficients. These coefficients are then rotated back into the xz-coordinate system by the angle ε as given by

$$\overset{xz}{\begin{bmatrix} C_l \\ C_d \end{bmatrix}} = \begin{bmatrix} \cos\varepsilon & -\sin\varepsilon \\ \sin\varepsilon & \cos\varepsilon \end{bmatrix}^{wind} \begin{bmatrix} C_l \\ C_d \end{bmatrix}, \tag{30}$$

where xz indicates the xz-coordinate system and wind indicates the local wind coordinate system.

Using the standard definitions of lift coefficient (C_L) and section lift coefficient (C_l),

$$C_L = \frac{L}{QS} \text{ and } C_l = \frac{l}{Qc}, \tag{31}$$

a straightforward integration of these coefficients over the entire wing gives the overall lift and pitching moments of the wing. Starting with the relation between lift and section lift

$$L = \int_{-b/2}^{b/2} l dy, \tag{32}$$

the lift coefficient can then be calculated by

$$C_L = \frac{1}{\hat{S}} \int_{-1}^{1} C_l \hat{c} d\eta, \tag{33}$$

Similarly, the drag coefficient is given by

$$C_D = \frac{1}{\hat{S}} \int_{-1}^{1} C_d \hat{c} d\eta. \tag{34}$$

In this problem formulation, side forces are considered negligible; therefore,

$$C_Y = 0\,. \tag{35}$$

The moment coefficients are also calculated in a straightforward manner. Starting from the definitions of pitch, roll, and yaw moment coefficients,

$$C_{\mathcal{M}} = \frac{\mathcal{M}}{QS\bar{c}},\ C_{\mathcal{L}} = \frac{\mathcal{L}}{QSb},\ \text{and}\ C_{\mathcal{N}} = \frac{\mathcal{N}}{QSb}, \tag{36}$$

respectively, the moment coefficients can be calculated using the section lift and drag coefficients as follows:

$$C_{\mathcal{M}} = \frac{1}{\hat{S}\hat{\bar{c}}}\int_{-1}^{1} C_l \hat{c}\xi d\eta\,,\ C_{\mathcal{L}} = \frac{1}{2\hat{S}}\int_{-1}^{1} C_l \hat{c}\eta d\eta\,,$$

$$C_{\mathcal{N}} = \frac{1}{2\hat{S}}\int_{-1}^{1} C_d \hat{c}\eta d\eta\,. \tag{37}$$

Two other important parameters in wing design are the centers of pressure and gravity. The displacement between these two points is very important in determining the stability and dynamic response of the wing in an unsteady flight condition and in determining the dynamics of the overall aircraft system. In the context of the prescribed geometry, the center of pressure relative to the origin is calculated as follows:

$$\begin{aligned} Lx_{cp} &= \mathcal{M} \\ x_{cp} &= \frac{1}{L}\int_{-b/2}^{b/2} l x_{c/4} dy \end{aligned}\,. \tag{38}$$

Similarly, the center of gravity is equal to

$$x_{cg} = \frac{\int_{-b/2}^{b/2} \sigma x dy}{\int_{-b/2}^{b/2} \sigma dy} = \frac{\int_{-b/2}^{b/2} c^2 x dy}{\int_{-b/2}^{b/2} c^2 dy} \tag{39}$$

Here, it is assumed that the density of the wing is constant, which leads to a square variation of mass with respect to chord length.

5. Results

Using the methods described in the previous section, circulation, downwash, and force distributions are calculated for several wing shapes, as well as overall wing parameters such as lift, drag, and center of pressure location. This method's relatively loose requirements for wing geometry enable some non-traditional wings to be analyzed. Along the vein of bio-inspiration, a gull wing shape is chosen as the basis of this analysis. This wing features forward- and aft-swept wing sections that can be utilized for c.g. and c.p. adjustments, as discussed below. The wing is described by the quarter-chord curve

$$x(y) = a\left[\left(\frac{y}{ky_0}\right)^4 - \left(\frac{y}{ky_0}\right)^2\right] \tag{40}$$

and shown in Figure 1.3 for various values of curvature parameter *a*. (A value of $k = \sqrt{3/7}$ is chosen in order to maintain a constant c.g. location for all values of *a*, assuming a constant density wing as described previously.)

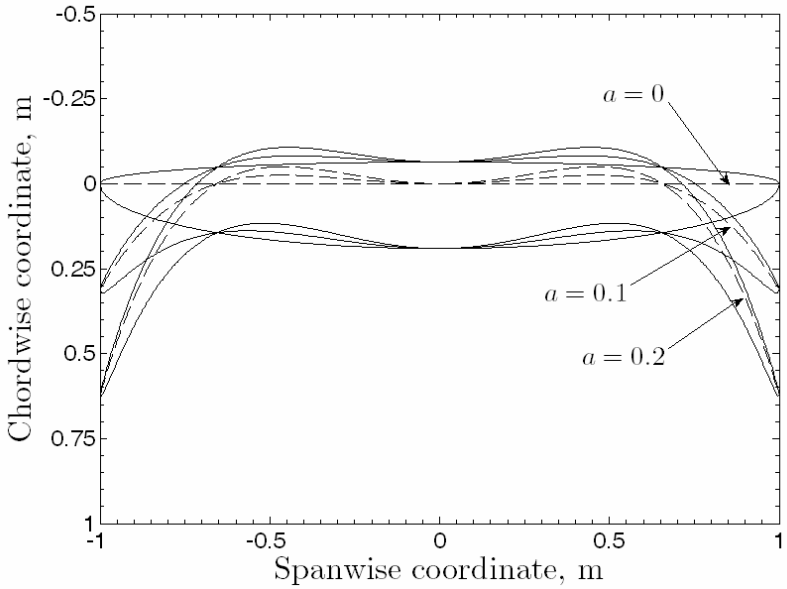

Figure 1.3: Gull wings of constant span with curvature parameter a = 0, 0.1, 0.2

For this analysis, every wing shape is constructed using an elliptical chord distribution such that a direct comparison of these wings with the canonical straight, elliptical wing can be made. Also, the same root chord length is used throughout in order to maintain a constant aspect ratio of 10. Although this analysis may be used for any angle of attack within the range of validity of linear theory, an angle of attack of 3° will be used subsequently as a point for comparison.

As an example, the three wings depicted in Figure 1.3 are analyzed using this lifting-line theory and compared in Figs. 4-7, using $m = M = 101$. Figure 1.4 shows the circulation distributions $\Gamma(y)$ for various values of curvature parameter a. As a increases, the circulation increases towards the center, where the wing behaves locally as a forward-swept wing, while towards the wingtips the aft sweep of the wing causes a local reduction in circulation, compared to the elliptical distribution of the straight wing case. The downwash angle $\varepsilon(y)$, computed from Eq. (39), is plotted in Figure 1.5. The downwash is nearly constant in the case of the straight elliptical wing (a =

0), as predicted by Prandtl [14] and Munk [13]. As the wing curvature increases, downwash on the forward-swept sections of the wing increases while decreasing across the aft-swept portions. Similar effects of swept curvature on downwash angle have been shown for parabolic wings by Prössdorf and Tordella. They note that the largest decrease in induced velocity occurs towards the wingtips [7].

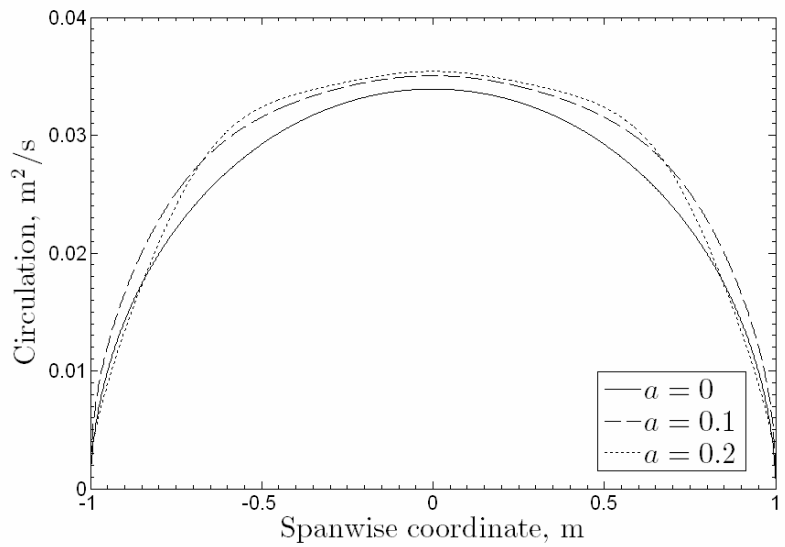

Figure 1.4: Circulation distribution of several gull wings, $\Lambda = 10$, $\alpha = 3°$

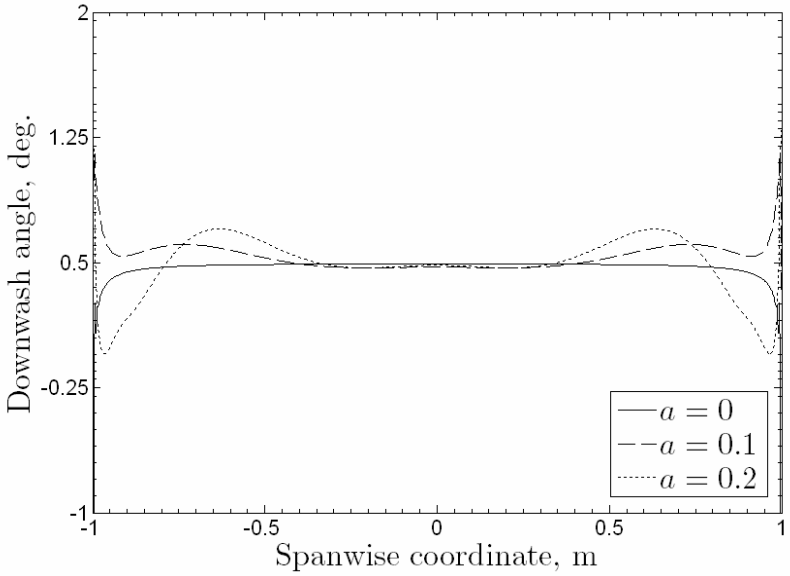

Figure 1.5: Downwash angle distribution of several gull wings, $\Lambda = 10$, $\alpha = 3°$

Figure 1.6 is a plot of the lift force per unit length distribution across the same three gull wings, while Figure 1.7 displays the drag force. As expected, the lift and drag distributions are both elliptical for the straight wing case. The lift distributions are approximately equal to the circulation distributions, scaled by a factor of ρU_∞, since in all cases the downwash angles are small. Similarly, the drag distributions follow the same patterns as the downwash angle distributions. These plots indicate the gull wing's ability to shift the center of lift forward as the wing morphs from straight to curved, although a drag penalty is incurred.

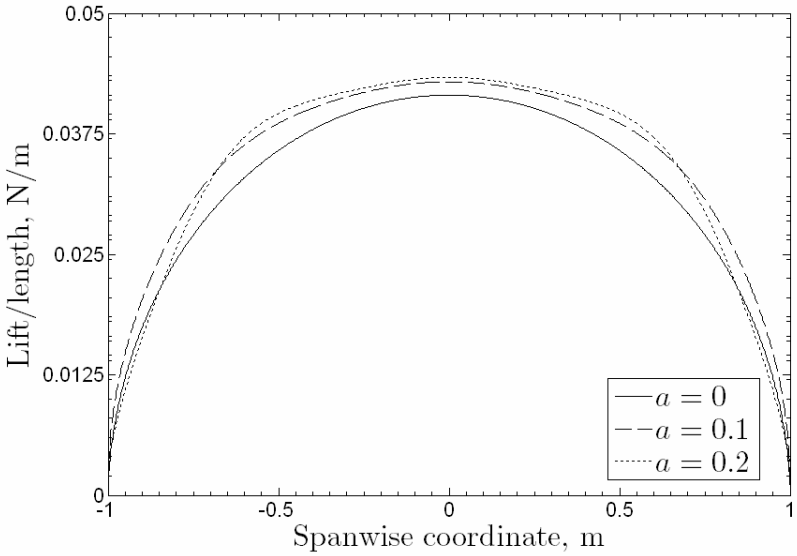

Figure 1.6: Lift per unit length distribution of several gull wings, $\Lambda = 10$, $\alpha = 3°$

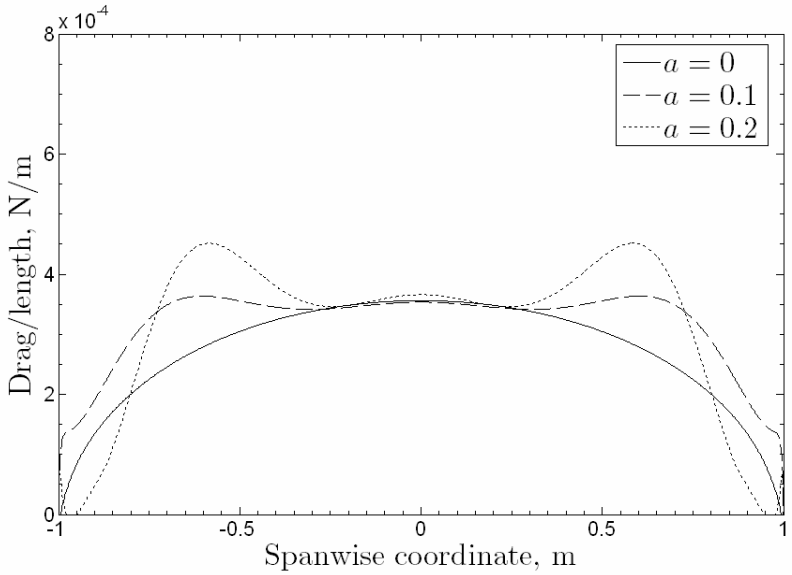

Figure 1.7: Drag per unit length distribution of several gull wings, $\Lambda = 10$, $\alpha = 3°$

The preceding comparison of several gull wings of constant span (and aspect ratio) is desired from a purely theoretical stance since aspect ratio is an important nondimensional parameter when discussing finite wings. For example, aspect ratio is a major factor in comparing the lift-to-drag ratios of several wings of similar shape. However, when developing and analyzing morphing wing designs, a constant aspect ratio is often difficult to maintain due to practical limits on planform deformation. Variable-swept wing aircraft such as the F-111 and the F-14 clearly exemplify the reduction in aspect ratio that morphing wing technologies suffer. To return to the previous example, Figure 1.8 depicts several gull wings of the same curvature parameters as before but now with constant arc length. These wings more clearly illustrate the deformations caused by bending a straight wing along the quarter-chord line in order to achieve a gull-like geometry. Once again these wings are curved in such a way as to maintain a constant center of gravity location. These wings are compared with the wings depicted in Figure 1.3 in Table 1.1 below.

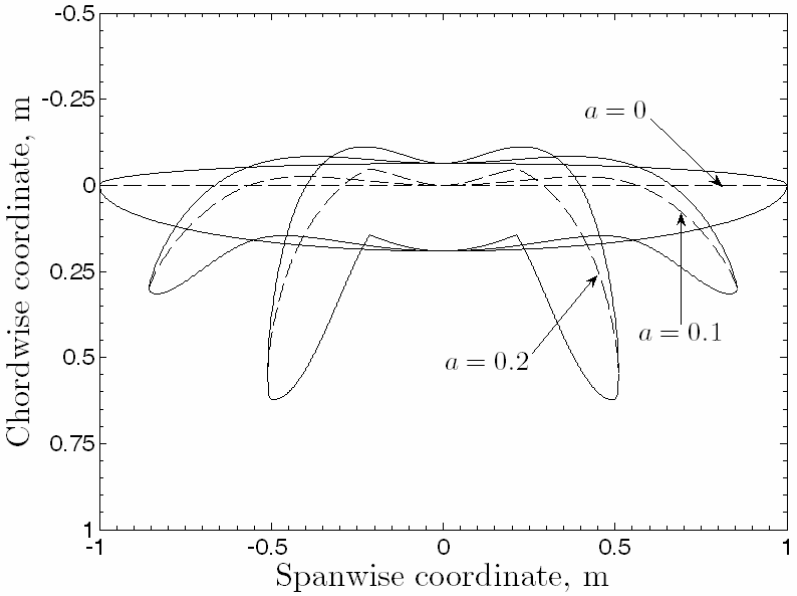

Figure 1.8: Gull wings of constant arc length with curvature parameter a = 0, 0.1, 0.2

Table 1.1: Comparison of several gull wings

	Wings of constant span			Wings of constant arc length		
a	Lift, N	Drag, N	Lift/Drag	Lift, N	Drag, N	Lift/Drag
0	0.0645	5.436e-4	118.6	0.0645	5.436e-4	118.6
0.1	0.0695	6.296e-4	110.3	0.063	7.287e-4	86.45
0.2	0.0688	6.248e-4	110.0	0.0417	8.999e-4	46.31

As expected, the wings of smaller aspect ratio have reduced lift-to-drag efficiency. This effect is much greater than merely changing the curvature of constant aspect ratio wings. Also note that there is a maximum in drag force within this range of curvature parameter for wings of constant span. Initially drag increases with curvature due to added downwash over the forward swept sections of the wing; however, at higher curvatures this is mitigated by the reduced downwash over the highly aft-swept wingtip sections.

As shown by Table 1.1, morphing a straight wing into a gull-like configuration is useful for lift reduction for higher speed flight. For example, a high endurance

reconnaissance aircraft may morph its wings by increasing their curvature parameter *a* in order to perform a high-speed dive in order to evade an enemy. The added feature of forward- and aft-swept wing sections allows the manipulation of the center of pressure if wing twist can be commanded as a function of span.

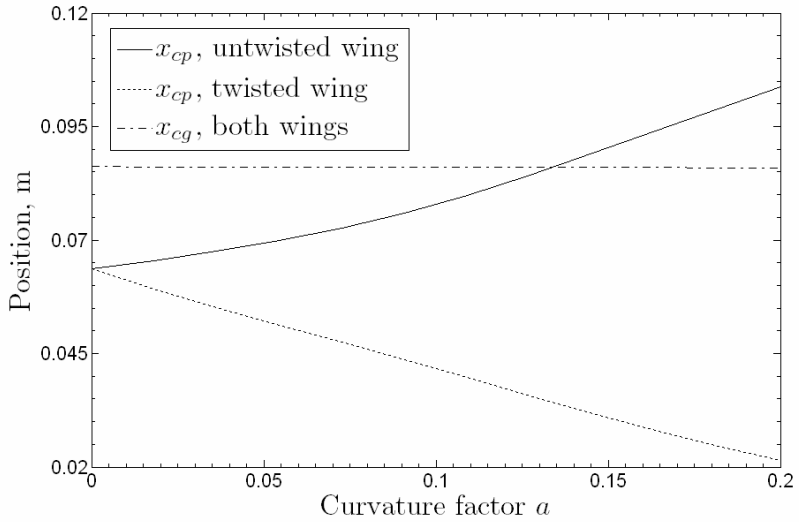

Figure 1.9: Variation in c.p. and c.g. for twisted and untwisted gull wings on the interval a = [0, 0.2], $\theta_{\max}$ = 5°

Figure 1.9 shows the variation in centers of pressure and gravity with curvature parameter for gull wings of constant wingspan. Untwisted wings, like those discussed above, are compared to twisted wings with twist distributions of the form

$$\theta(y) = \theta_{\max} \sin\left(\frac{\pi}{k}|y|\right), \tag{41}$$

where once again $k = \sqrt{3/7}$. Figure 1.9 indicates that with a maximum twist of only 5 degrees, the center of pressure can be shifted forward by 18% of the root chord while not moving the center of gravity. Thus, a change in wing configuration from straight to gull can be used to reduce the static margin of the aircraft, for example.

6. Conclusion

An extension of Weissinger's method to curved wings provides a useful analysis tool for the preliminary design of morphing wings. This method can be easily applied to wings whose geometry can be described by piecewise analytical functions. The analytical nature of this technique allows specific geometrical parameters to be varied and their effects on the wing's aerodynamics to be analyzed; however, caution must be taken when considering flows where viscous effects dominate. In this chapter, a morphing gull wing is analyzed in the cases of both constant span and constant arc length. It is shown that increased curvature of the wing results in reduced lift and lift-to-drag efficiency, confirming this morphology's usefulness in loiter to high-speed dash reconfiguration. Also, this wing's ability to manipulate its center of pressure location relative to its center of gravity is discussed. Each of these studies demonstrates the usefulness of this analysis technique, as long as the bounds of this method's validity are not overstepped.

REFERENCES

[1] Sanders, B., Crowe, R., and Garcia, E., "Defense Advanced Research Projects Agency—Smart Materials and Structures Demonstration Program Overview," *Journal of Intelligent Material Systems and Structures*, Vol. 15, 2004, pp. 227–233.

[2] Bowman, J., Sanders, B., and Weisshaar, T., "Evaluating the Impact of Morphing Technologies on Aircraft Performance," AIAA Paper 2002-1631, 2002.

[3] Wickenheiser, A., Garcia, E., and Waszak, M., "Evaluation of Bio-Inspired Morphing Concepts with Regard to Aircraft Dynamics and Performance," *Proceedings of SPIE—The International Society for Optical Engineering*, Vol. 5390, 2004, pp. 202–211.

[4] McGowan, A. R., "AVST Morphing Project Research Summaries in FY 2001," NASA TM-211769-2002, 2002.

[5] Wickenheiser, A., Garcia, E., and Waszak, M., "Longitudinal Dynamics of a Perching Aircraft Concept," *Proceedings of SPIE—The International Society for Optical Engineering*, Vol. 5764, 2005, pp. 192–202.

[6] Weissinger, J., "The Lift Distribution of Swept-Back Wings," NACA TM-1120, 1947.

[7] Prössdorf, S., and Tordella, D., "On an Extension of Prandtl's Lifting Line Theory to Curved Wings," *Impact of Computing in Science and Engineering*, Vol. 3, No. 3, 1991, pp. 192–212.

[8] Chiocchia, G., Tordella, D., and Prössdorf, S. "The Lifting Line Equation for a Curved Wing in Oscillatory Motion," *Zeitschrift fuer Angewandte Mathematik und Mechanik*, Vol. 77, No. 4, 1997, pp. 295–315.

[9] DeYoung, J., and Harper, C. W., “Theoretical Symmetric Span Loading at Subsonic Speeds for Wings Having Arbitrary Plan Form,” NACA Report No. 921, 1948.

[10] Multhopp, H.. “Die Berechnung der Auftriebsverteilung von Tragflgeln (The Calculation of the Lift Distribution of Wings),” *Luftfahrtforschung*, Vol. 15, 1938, pp. 153–169 (translated as British RTP translation No. 2392).

[11] Glauert, H., *The Elements of Aerofoil and Airscrew Theory*, The University Press, Cambridge, 1943.

[12] Munk, M. M., “The Minimum Induced Drag of Airfoils,” NACA Report 121, 1921.

[13] Prandtl, L., *Essentials of Fluid Dynamics*, Hafner Publishing Company, New York, 1952, pp. 206–215.

This chapter originally appeared as:

Wickenheiser, A., and Garcia, E., “Aerodynamic Modeling of Morphing Wings Using an Extended Lifting-Line Analysis,” *Journal of Aircraft*, Vol. 44, No. 1, 2007, pp. 10-16.

CHAPTER 2
LONGITUDINAL DYNAMICS OF A PERCHING AIRCRAFT[1]

1. Abstract

This chapter introduces a morphing aircraft concept whose purpose is to demonstrate a new bio-inspired flight capability: perching. Perching is a maneuver that utilizes primarily aerodynamics – as opposed to thrust generation – to achieve a vertical or short landing. The flight vehicle that will accomplish this is described herein with particular emphasis on its addition levels of actuation beyond the traditional aircraft control surfaces. The dynamics of this aircraft are examined with respect to changing vehicle configuration and flight condition. The analysis methodologies include an analytical and empirical aerodynamic analysis, trim and stability analyses, and flight simulation. For this study, the aircraft's motions are limited to the longitudinal plane only. Specifically, cruise and the perching maneuver are examined, and comparisons are drawn between maneuvers involving vehicle reconfiguration and those that do not.

2. Introduction

One of the major goals of the morphing aircraft program is the enabling of new flight capabilities and missions [1-3]. With additional levels of sensing and actuation, morphing aircraft are able to mimic more closely the capabilities of man's inspiration for flight: birds. The gross extents to which birds morph their bodies allow them to perform maneuvers irreproducible by conventional aircraft. One such avian maneuver is perching. Perching can be described as a high angle-of-attack approach, with the

[1] From Wickenheiser, A. and Garcia, E., "Longitudinal Dynamics of a Perching Aircraft"; reprinted by permission of the American Institute of Aeronautics and Astronautics, Inc.

purpose of using high-drag, separated flow for braking, followed by a vertical or very short landing [4]. This maneuver is based off of several avian landing techniques, including maximizing drag by flaring the wings and tail, and diving under the intended landing site and then pulling up into a climb to reduce speed. While vertical landings have been accomplished by rotary and V/STOL aircraft, it is desired to perch using primarily aerodynamics, with little input from thrust-generating devices. This will alleviate the need for the heavy thrust generators required to land vertically, which are not compatible with long endurance aircraft systems. Thus, perching will be especially useful for small, efficient reconnaissance aircraft, for example, whose thrust-to-weight ratios might be on the order of 1/10.

This chapter presents a concept for a perching aircraft and an analysis of its longitudinal dynamics. This concept is based on the Aerial Regional-Scale Environmental Survey (ARES) Mars scout craft, an aircraft designed to unfold from a Viking derivative aeroshell and fly for approximately 70 minutes over a Martian landscape, collecting data on atmospheric chemistry, geology, and crustal magnetism [5]. The idea to try to perch a similar airframe grew from the challenge to save the ARES scout from a high-speed crash landing at the end of its mission by using drag to slow it down enough to land with its instruments intact. It is desired to perform the perching maneuver without complicating the aircraft system unnecessarily and by adding the fewest number of additional actuators. The original ARES craft features a blended-wing body with folding tail boom, tail surfaces, and wings, shown in Figure 2.1. The inverted V-tail features two ruddervators that combine the functionality of a rudder and elevator. In order to add perching capabilities, actuators are incorporated into the tail degrees of freedom, and variable incidence is added to the folding wing

sections. These additional degrees of actuation in the perching flight vehicle, dubbed the ARES-C, are shown in Figure 2.2.

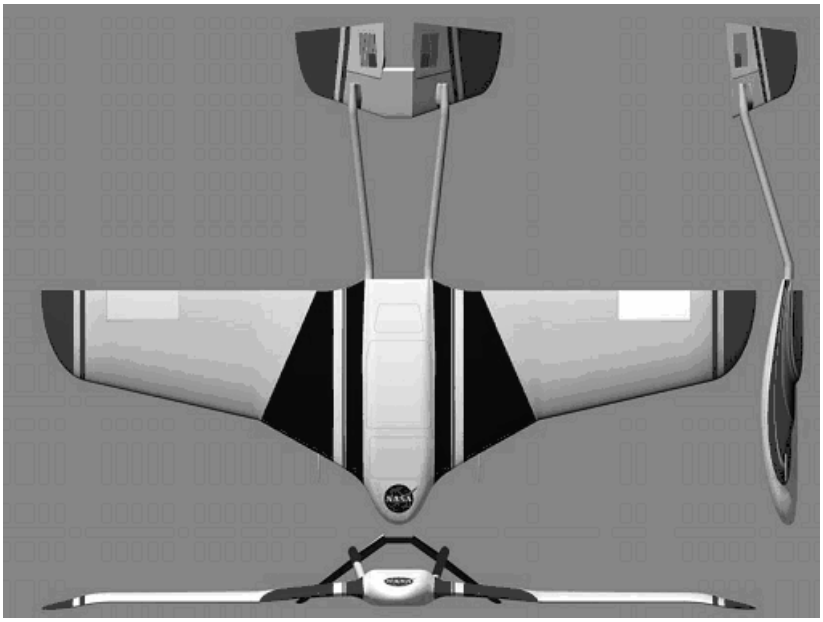

Figure 2.1: The ARES Mars scout [13]

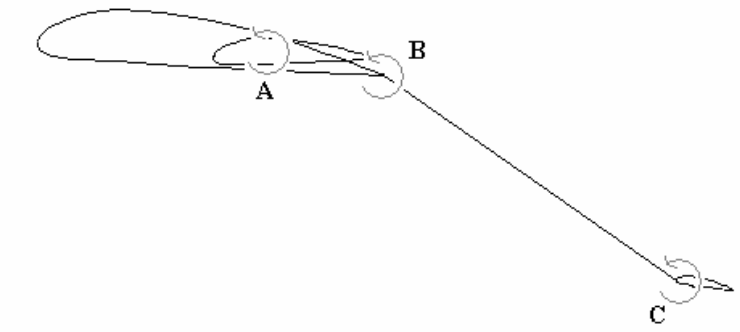

Figure 2.2: The three primary actuations about the pitch axis: A) rotation of the wing incidence angle with respect to the fuselage body axis, B) rotation of the tail boom, and C) rotation of the horizontal stabilizer

The level of geometric reconfigurability required to recreate the perching maneuver in a manmade aircraft falls far outside the bounds of conventional aircraft designs. In order to maintain stability and controllability at the high angles of attack required for aerodynamic braking, the aircraft's wings are rotated to a negative incidence angle in order to moderate their angle of attack with respect to the oncoming air as the body's angle of attack increases past stall. Additionally, the tail is rotated down and out of the resulting unsteady wake of the body, and the horizontal stabilizer is also actuated in order to remain in the linear angle of attack range as the tail boom rotates. These actuations keep the standard aileron and ruddervator surfaces effective at trimming and control. They also allow a larger degree of control over the aircraft's dynamics through a wider range of flight conditions.

For the purposes of this initial study, the aircraft is modeled in the longitudinal plane only; that is, roll, yaw, and sideslip dynamics are not considered. By eliminating lateral dynamics, the number of parameters in the aerodynamic model is greatly reduced, and asymmetric geometric configurations need not be considered. Also, it is assumed a priori that the optimal perching trajectory, in terms of curvilinear distance, time to land, or overall energy consumption, will be confined to the longitudinal plane. Even restricted to this plane, lateral dynamics enter into the model when considering post-stall aerodynamics, which feature asymmetric flows, and disturbance rejection from sideslip wind gusts; however, both of these phenomena are beyond the scope of this study.

In the present aerodynamic model, the fuselage and wings are modeled as a blended-wing body, and the tail is considered as a separate lifting surface. The aerodynamic forces on the aircraft components are calculated using a modified version of

Weissinger's method [6]. This analysis assumes that the wing quarter-chord line and chord distribution are expressed as an arbitrary function of the span; it is not restricted to straight-swept wings. However, this method assumes no sideslip, which is a reason why this analysis is restricted to the longitudinal plane only. Also, this theory assumes small angles of attack; thus high-angle-of-attack, separated flow is not considered here. The advantages of using an analytical method such as this are its speed and reconfigurability. It allows the computation of aerodynamic properties of non-conventional wing geometries, such as those of this perching aircraft, in a matter of minutes, compared to the hours or days a computational fluid dynamics (CFD) analysis would require. Also, the quarter-chord curves, chord distributions, and twist distributions are input as piecewise analytical functions of the span coordinate; therefore, the wing geometry may be easily and quickly modified between aerodynamic analyses to account for aircraft reconfigurations.

This aerodynamic model of the aircraft is used to study the longitudinal dynamics of the vehicle and to simulate the perching maneuver. Specifically, the variation of the trim conditions as the shape morphs is discussed. The linearized dynamics around these trim points – the dynamic modes – are analyzed for stability using standard linear system analyses. Analyses of the cruise configuration as well as the initiation of the perching maneuver are presented, both within the range of validity of the aerodynamic model. The longitudinal dynamics of this shape change are simulated using a nonlinear three-degree-of-freedom aircraft simulation developed in the Simulink programming environment.

All dimensional results presented herein refer to a prototype of the ARES-C that was fabricated at Cornell in 2004. The aircraft's wingspan (tip to tip) is approximately 2 meters, and its weight is approximately 40 Newtons.

3. Problem Formulation

In order to predict the dynamics of the ARES-C, first an accurate model of the aerodynamic forces is developed for various vehicle configurations and flight conditions. This model is an extended lifting-line model based off of Weissinger's method for straight, swept wings. This analysis method also incorporates real airfoil force data, which may be obtained from CFD programs or wind tunnel experiments. This is accomplished by following the reasoning of DeYoung and Harper [7], who suggest the method of distorting the chord length distribution along the wing such that the dimensional circulation about every span station matches the dimensional circulation of an ideal airfoil with the original chord length. This correction for real airfoils may alternatively be factored in by adjusting the wing incidence angle along the span.

In order to match closely the aerodynamics of the ARES craft, airfoils whose lift-to-drag characteristics resemble the ARES' airfoils' [8] are selected for the ARES-C. This is accomplished by analyzing the ARES' airfoils using a CFD analysis, computed using Fluent, that simulates the Mars environment. A catalog of low-speed airfoil data, provided by the University of Illinois at Urbana-Champaign [9], is referenced in order to choose these airfoils. As with the ARES, three airfoils are chosen: one for the fuselage centerline, one for the wing root, and one for the wing tip. In between these span stations, the wing cross sections are lofted (i.e. interpolated) linearly. The lift

data gathered for the three selected airfoils are presented in Figure 2.3, and their span locations on the ARES-C are shown in Figure 2.4.

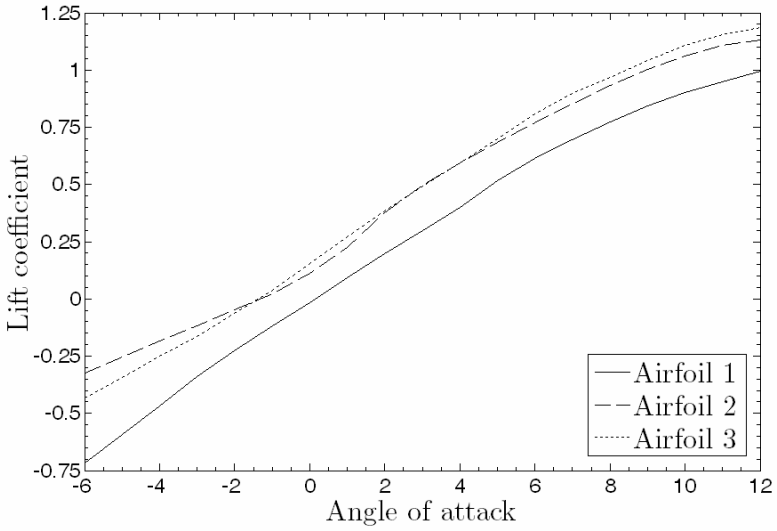

Figure 2.3: Lift curves of ARES-C airfoils

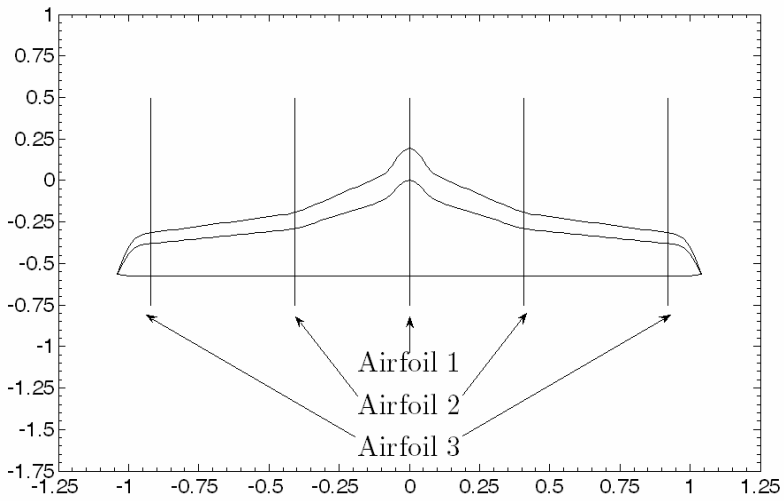

Figure 2.4: ARES-C airfoil span locations

This aerodynamic analysis is used to generate lookup tables for a longitudinal simulation of the ARES-C. Consequently, the simulation is only valid in the range of

the airfoil data given in Figure 2.3 and the moderate angle of attack regime of lifting-line theory. The dynamics of the ARES-C are governed by the traditional equations of motion for aircraft:

$$\frac{dm}{dt}\mathbf{v} + m\frac{d\mathbf{v}}{dt} + \boldsymbol{\omega}\times m\mathbf{v} = \mathbf{f} + m\mathbf{T}\mathbf{g} \tag{1}$$

$$\frac{d\mathbf{x}}{dt} = \mathbf{T}^T\mathbf{v} \tag{2}$$

$$\frac{d\mathbf{I}}{dt}\boldsymbol{\omega} + \mathbf{I}\frac{d\boldsymbol{\omega}}{dt} + \boldsymbol{\omega}\times\mathbf{I}\boldsymbol{\omega} = \mathbf{m} \tag{3}$$

$$\dot{\mathbf{q}} = \frac{1}{2}\begin{bmatrix} 0 & -\boldsymbol{\omega} \\ \boldsymbol{\omega} & \boldsymbol{\omega}^{\times} \end{bmatrix}\mathbf{q} \tag{4}$$

Note the special consideration in Eq. (3) for a time-varying moment of inertia matrix. Also note that the forces and moments are given in local (non-inertial) aircraft body coordinates so that aerodynamic data may be used from the lifting-line analysis. The subsequent analyses only consider the longitudinal dynamics, so the side force, roll, and yaw equations are disregarded. Thus, the above set of 13 equations (Eqs. (1)-(4)), is reduced to the following set of six scalar equations:

$$\dot{u} = \frac{1}{m}\left(f_x - \dot{m}u\right) - wq - g\sin\theta \tag{5}$$

$$\dot{w} = \frac{1}{m}\left(f_z - \dot{m}w\right) + uq + g\cos\theta \tag{6}$$

$$\dot{x} = u\cos\theta + w\sin\theta \tag{7}$$

$$\dot{z} = -u\sin\theta + w\cos\theta \tag{8}$$

$$\dot{q} = \frac{1}{I_y}\left(m_y - \dot{I}_y q\right) \tag{9}$$

$$\dot{\theta} = q \tag{10}$$

In order to analyze the change in aircraft trim states under various flight conditions and geometrical configurations, the derivatives in the above equations of motion are zeroed, and the steady-state conditions are obtained as follows:

$$0 = m_y \tag{11}$$

$$0 = f_z + mg\cos\theta \tag{12}$$

$$0 = f_x - mg\sin\theta \tag{13}$$

Written in terms of aerodynamic forces and moments, these equations become

$$0 = \mathcal{M}(\alpha, \delta_e, \delta_a, V) \tag{14}$$

$$0 = -D(\alpha, \delta_e, \delta_a, V)\sin\alpha - L(\alpha, \delta_e, \delta_a, V)\cos\alpha + mg\cos\theta \tag{15}$$

$$0 = -D(\alpha, \delta_e, \delta_a, V)\cos\alpha - L(\alpha, \delta_e, \delta_a, V)\sin\alpha - mg\sin\theta + T \tag{16}$$

where parameter dependence is noted for the lift, drag, and pitching moment terms. Other morphing parameters, such as wing incidence or tail boom angle, are not present: they are not considered to be dependent variables in trimming the aircraft. Note that symmetric ruddervator deflection is denoted δ_e, here and throughout the rest of this chapter, since its use is synonymous with elevator deflection. The angle of attack and aileron deflection angle are fixed in order to calculate the trim condition at those angles. This will determine if the aircraft is "flyable"; that is if it can be trimmed at every angle of attack during cruise. This will also allow the geometrical state of the aircraft to be treated as an independent variable, such that the dynamics of the aircraft can be described as functions of the morphing parameters. This system of nonlinear equations is triangular, meaning it can be solved sequentially in the order given. Although Eq. (14) still depends on both elevator deflection and velocity, the trim elevator position does not depend on the vehicle's velocity in the linear

aerodynamic range, since in this regime changes in velocity scale the load distribution between the wings and tail uniformly. Subsequently, Eq. (15) can be solved for velocity, and Eq. (16) can be solved for thrust.

In order to study the stability of these trim conditions as the flight condition and geometrical configuration change, the equations of motion are linearized about each trim point. This is accomplished through the usual Taylor Series expansion of the forces and moments, yielding the following linear system of longitudinal dynamics equations [10]:

$$\frac{d}{dt}\begin{pmatrix} u/V \\ \alpha \\ q \\ \theta \end{pmatrix} = \begin{bmatrix} X_u & \frac{X_\alpha}{V} & 0 & \frac{-g\cos\Theta_0}{V} \\ \frac{VZ_u}{V-Z_{\dot\alpha}} & \frac{Z_\alpha}{V-Z_{\dot\alpha}} & \frac{V+Z_q}{V-Z_{\dot\alpha}} & \frac{-g\sin\Theta_0}{V-Z_{\dot\alpha}} \\ VM_u + \frac{VZ_uM_{\dot\alpha}}{V-Z_{\dot\alpha}} & M_\alpha + \frac{VZ_uM_{\dot\alpha}}{V-Z_{\dot\alpha}} & M_q + \frac{(V+Z_q)M_{\dot\alpha}}{V-Z_{\dot\alpha}} & \frac{-M_{\dot\alpha}g\sin\Theta_0}{V-Z_{\dot\alpha}} \\ 0 & 0 & 1 & 0 \end{bmatrix} \begin{pmatrix} u/V \\ \alpha \\ q \\ \theta \end{pmatrix} + \begin{bmatrix} \frac{X_{\delta_e}}{V} \\ \frac{Z_{\delta_e}}{V-Z_{\dot\alpha}} \\ M_{\delta_e} + \frac{VZ_{\delta_e}M_{\dot\alpha}}{V-Z_{\dot\alpha}} \\ 0 \end{bmatrix} \delta_e \tag{17}$$

In Eq. (17), subscripted variables indicate with respect to which variable each force or moment is differentiated. Here, the derivatives $X(\cdot)$ and $Z(\cdot)$ are of the aircraft body forces fx and fz, respectively. The rotary derivatives $(\cdot)_u$ and acceleration derivatives $(\cdot)_\alpha$ are estimated using empirical relations given in the USAF Data Compendium (Datcom) [11] based on the static data computed with the aforementioned lifting-line method. For each trim condition, a new plant matrix given by Eq. (17) is computed

using the aerodynamic lookup tables and Datcom methods. The dynamic mode shapes and natural frequencies can then be computed straightforwardly from the plant matrix. A Simulink model of the dynamics of the perching aircraft is developed in order to simulate the trajectory of the aircraft as it morphs from a cruise configuration to the initiation of the perching maneuver. This model is designed to be expandable and modular so that various morphing vehicles or sets of aerodynamic data may be run in the same simulator. A schematic of this simulator appears in Figure 2.5, based off of a standard six-degree-of-freedom simulation [12].

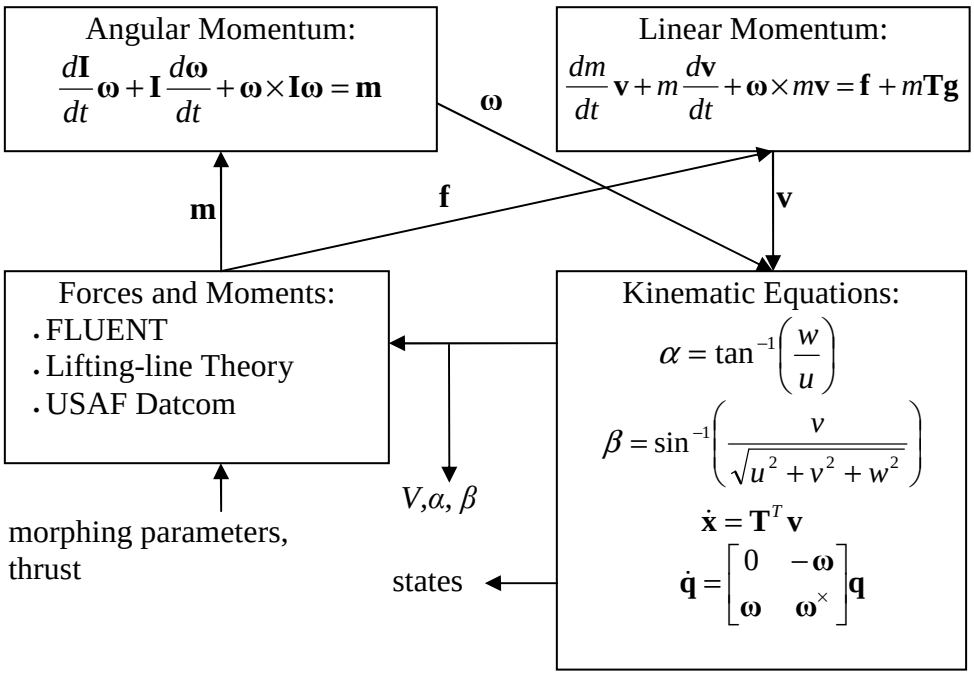

Figure 2.5: Overview of morphing aircraft simulator

This diagram shows the cyclical nature of the simulation process. Morphing parameters, such as wing incidence angle and tail boom angle, are the generalized inputs to this system, augmenting traditional inputs such as elevator or rudder deflections. The aforementioned lifting-line theory and Datcom methods are used to

determine the aerodynamic forces and moments on the aircraft at each step during its flight based on the current flight condition and vehicle configuration. These forces and moments determine the change in aerodynamic state for the next iteration. This model uses the quaternion representation for the heading angles and a 4^{th}-5^{th} order Runge-Kutta method for the numerical integration.

4. Results

In order to simulate how the aircraft morphs through variation shape configurations and flight conditions, a look-up table of the aerodynamic loads in terms of every varying parameter is constructed. These parameters are listed in Table 2.1 and are defined in Figure 2.6.

Table 2.1: Parameter variations in aerodynamic database

α	angle of attack	-5° – 15°
ι	wing incidence angle	-15°– 0°
θ_b	tail boom angle	-15°– 45°
θ_t	tail incidence angle	-5°– 15°
δ_a	symmetric aileron deflection angle	-20°– 20°
δ_e	symmetric ruddervator deflection angle	-20°– 20°

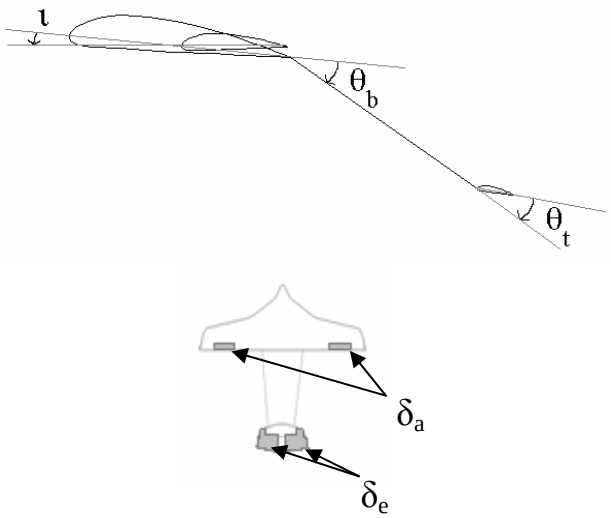

Figure 2.6: ARES-C morphing parameters

The speed and reconfigurability of the aforementioned lifting-line theory are utilized in the construction of this table: the over 9500 combinations of geometry and flight conditions used in the simulation can be tabulated in a matter of days. Some results of this analysis on the tail are presented in Figure 2.7, and the results from the blended wing-body are presented in Figure 2.8.

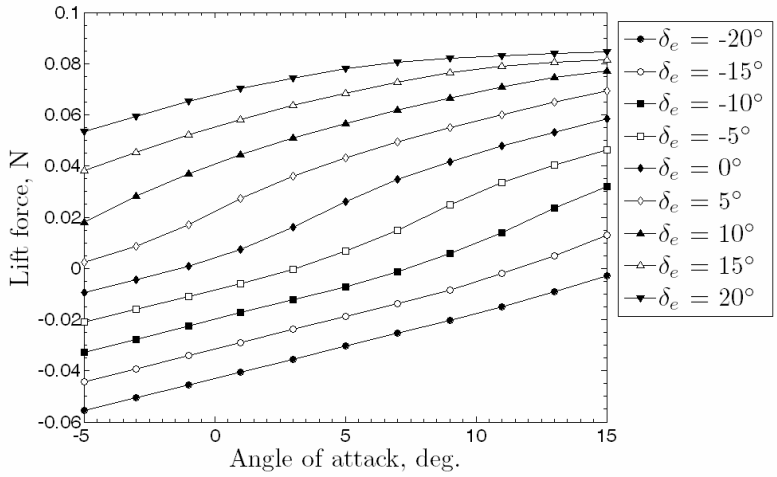

(a)

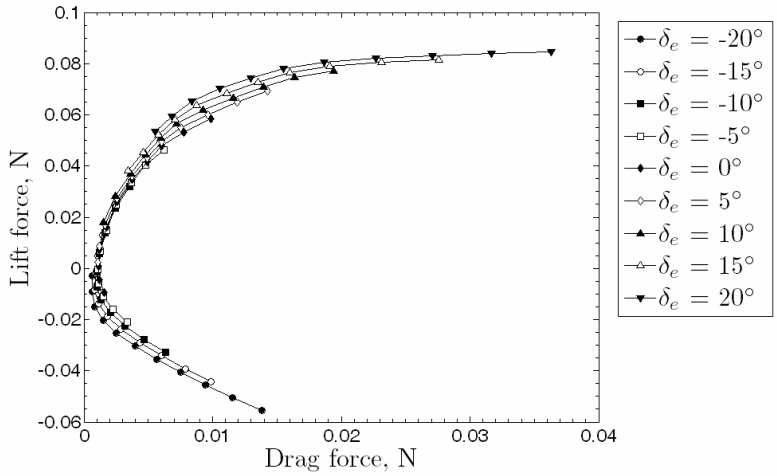

(b)

Figure 2.7: Aerodynamic data on the tail calculated by the modified Weissinger's method

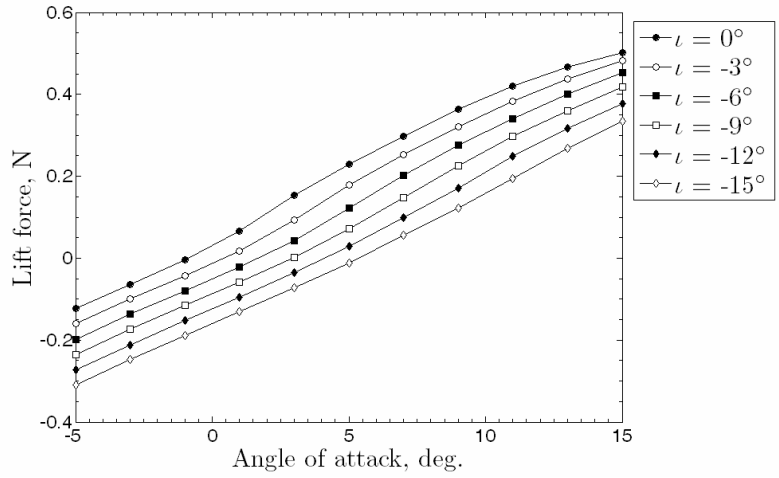

(a)

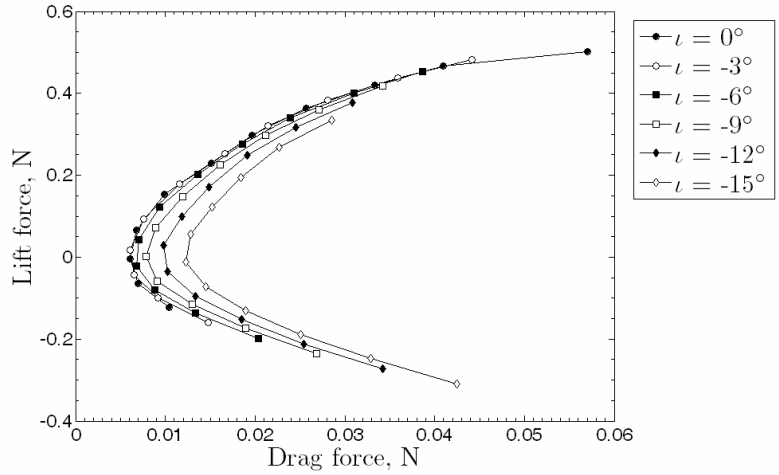

(b)

Figure 2.8 Aerodynamic data on the blended wing-body calculated by the modified Weissinger's method

Figure 2.7(a)-(b) shows the variation of the tail loads as function of angle of attack and symmetric ruddervator deflection. These plots show that the ruddervators start to lose their effectiveness at high deflections and angles of attack due to flow separation introduced by the experimental airfoil data. Also note in Figure 2.7(b) that there is very little difference between tail incidence and ruddervator deflection, since the ruddervators comprise about 75% of the tail's planform area. Figure 2.8(a)-(b) depicts the variation of aerodynamic loads on the fuselage blended wing-body as the angle of

attack and wing incidence angle change. This analysis predicts that drag increases and lift decreases uniformly as the negative wing incidence increases, as expected. Also, the minimum drag increases significantly as the wings are rotated, since at no point is the entire blended wing-body at the angle of attack for minimum drag. Thus, this geometrical change is shown to be effective in the initiation of the perching maneuver. This lookup table of aerodynamic data is used in the longitudinal dynamics simulation and analysis of the ARES-C. In order to determine the flight-worthiness of the aircraft, it is desired to trim the craft at every point within the linear range of angles of attack, with or without use of symmetric aileron deflection. These results for various angles of attack and symmetric aileron (i.e. flaperon) deflections are presented in Figure 2.9.

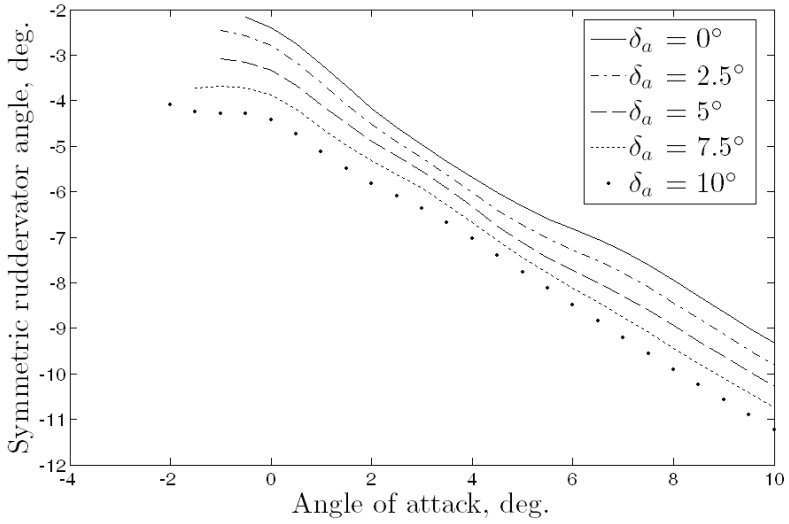

(a)

Figure 2.9: Trim results for various angles of attack and symmetric aileron (flaperon) deflections

Figure 2.9 (Continued)

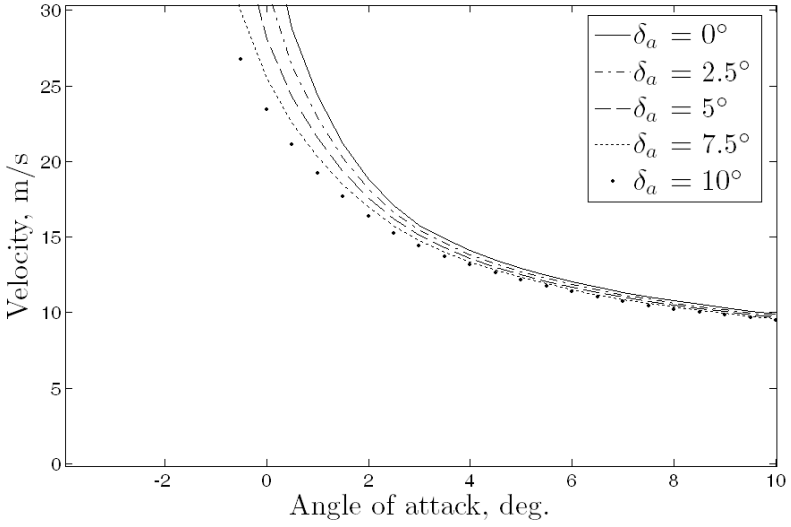

(b)

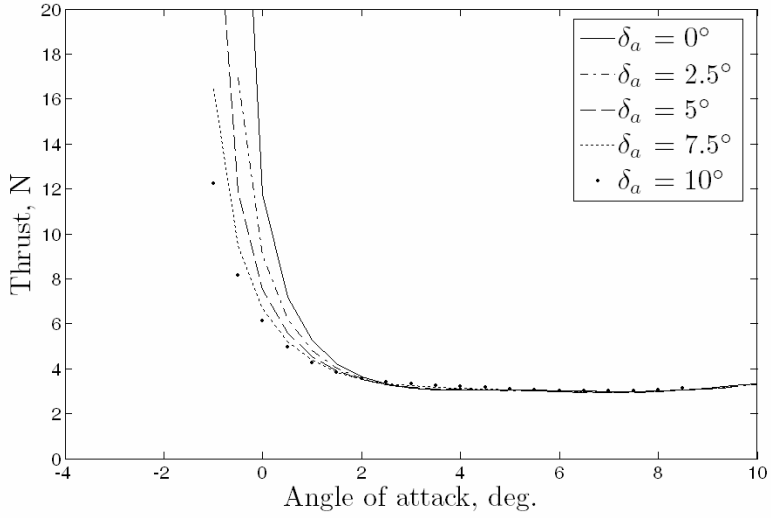

(c)

Figure 2.9 (Continued)

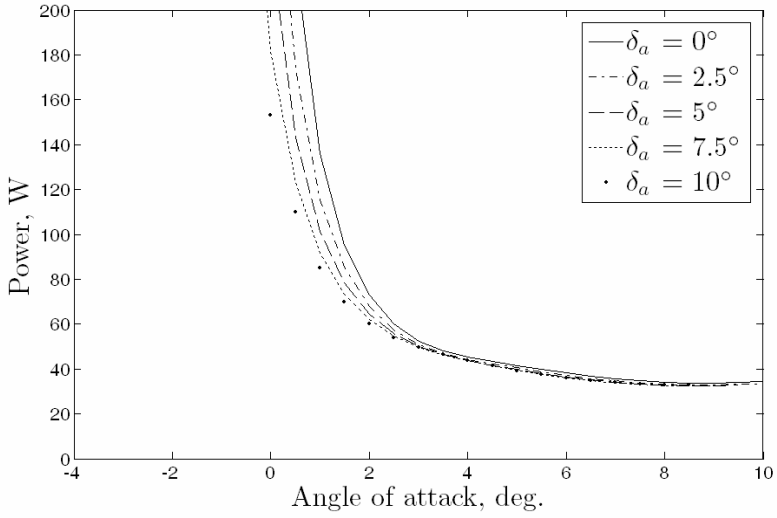

(d)

These plots indicate that the ARES-C follows the trends of standard aircraft. More ruddervator deflection is needed to trim at higher angles of attack, and minor flaperon deflection is needed to trim at negative angles of attack through adding slight "camber" to the wings. Naturally, the trim velocity decreases as angle of attack increases due to increased lift generation by the wings and fuselage. Finally, the trim thrust has a minimum around 3-4 degrees angle of attack for positive flaperon deflections. All conditions correspond to a trim thrust-to-weight ratio of around 1/10. The angle of attack for minimum power occurs between 7-9 degrees, with the higher angles corresponding to lower trim flaperon deflections. In terms of performance, the minimum thrust corresponds to the maximum range, whereas the minimum power corresponds to the maximum endurance.

The stability of each trim condition is analyzed by plotting the migration of the eigenvalues of the plant matrix given by Eq. (17). The entries of this matrix are

recomputed for each flight condition using a combination of table lookups and Datcom formulas.

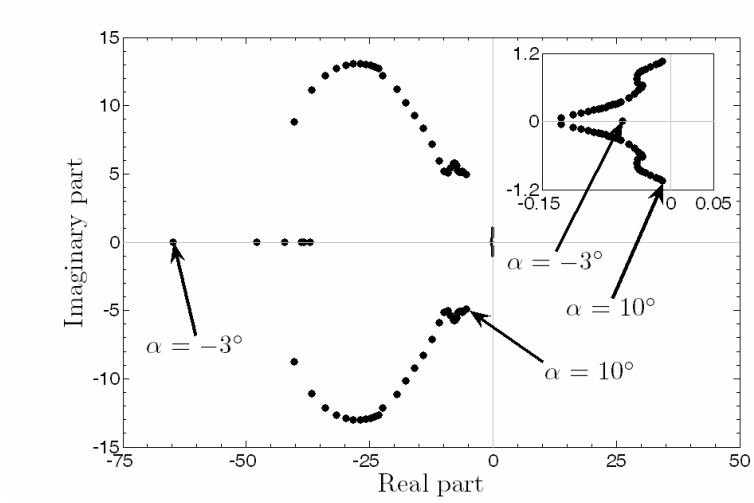

Figure 2.10: Eigenvalue migration as trim angle of attack varies (δ_a = 5°)

Figure 2.10 shows the migration of the aircraft's longitudinal eigenvalues as angle of attack varies from -3 – 10 degrees. For most trim conditions, there are two pairs of complex conjugate eigenvalues corresponding to the short-period and phugoid modes of pitch oscillation. The short-period mode can be described as a rapid, highly damped pitch oscillation, whereas the phugoid mode is a long-period, lightly damped porpoising mode with very little angle of attack variation. As shown, the short-period mode becomes less stable at higher angles of attack due to decreased effectiveness of the tail at creating restoring moments. At negative angles of attack, these oscillations disappear. One of the overdamped modes approaches instability due to the decrease in restoring moment by the wings.

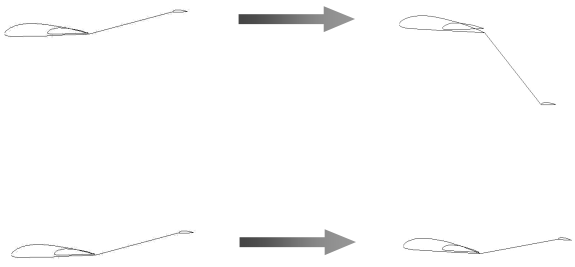

(a)

(b)

Figure 2.11: Maneuvers for comparison: (a) initiation of perching, (b) pitch up

The variation of the longitudinal dynamics as the perching maneuver is initialized is also examined. This maneuver consists of a wing incidence rotation by 5º and a rotation of the tail boom downward by 60º, as shown in Figure 2.11(a). This maneuver is compared to a standard speed reduction through pitching up the nose, with no geometrical reconfiguration, as shown in Figure 2.11(b). Both of these maneuvers result in an increase in the fuselage angel of attack from 0° to 5°. Figure 2.12 depicts the change in trim condition (symmetric ruddervator deflection, velocity, and thrust) throughout the maneuvers.

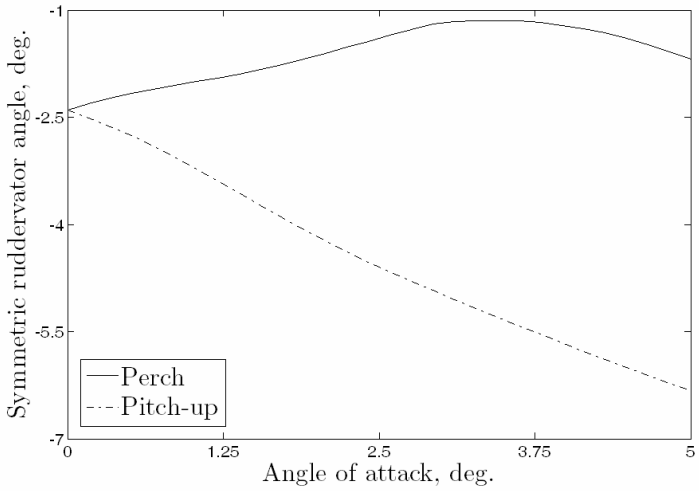

(a)

Figure 2.12: Change in trim conditions throughout the maneuvers

Figure 2.12 (Continued)

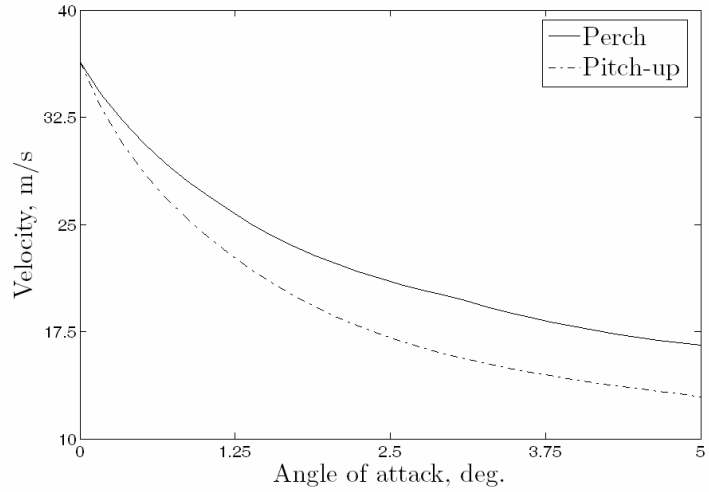

(b)

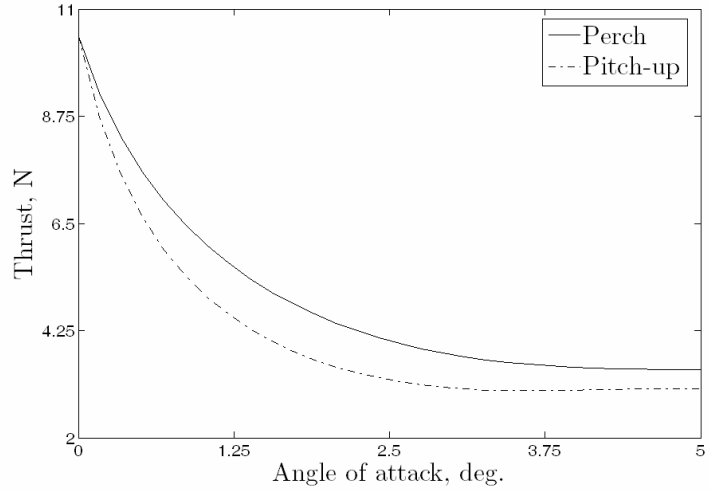

(c)

Figure 2.12 indicates that both maneuvers result in a reduction in cruise velocity and thrust, with the reduction resulting from the pitch-up being greater than the perching maneuver. However, the trim deflection of the ruddervator is much greater in the pitch-up case, meaning that it becomes less useful in trimming and controlling the aircraft at higher pitch angles. This example highlights one of the advantages of vehicle reconfiguration: the control surfaces remain highly effective under various

flight conditions. Here, the trim position of the ruddervators remains relatively unchanged as the vehicle's angle of attack increases.

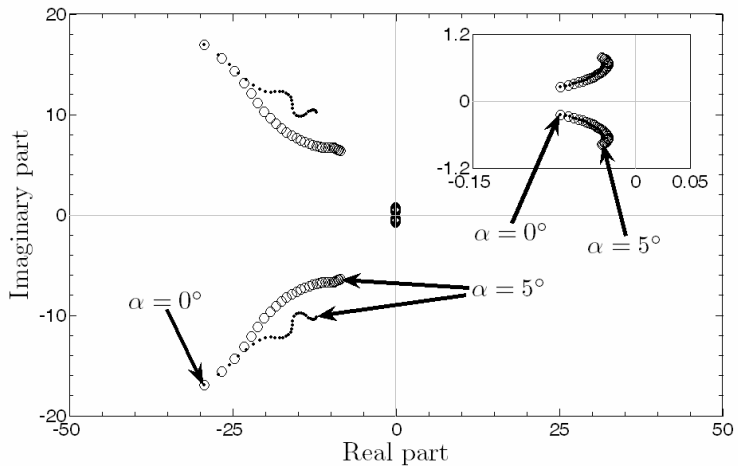

Figure 2.13 Eigenvalue migration throughout the maneuvers: the initiation of perching (○), pitch-up (·)

The short-period mode is affected the greatest during these maneuvers; the natural frequency of this mode is decreased in both cases due to the reduction in tail effectiveness at high angles of attack. In both cases, the eigenvalues approximately move along lines of constant damping. Damping is reduced during the initiation of the perching maneuver due to the reduction in the tail moment arm during the rotation of the tail boom. The differences in eigenvalue migrations seen in Figure 2.13 can therefore be most attributed to the manipulation of center of pressure, and to a lesser extent, center of gravity, that the geometrical reconfiguration of the perching maneuver accomplishes.

In order to simulate these maneuvers, it is assumed that the aircraft passes through a series of quasi-static trim conditions as the geometry morphs. These conditions are calculated using the previously described trim analysis. The morphing parameters and

control deflections needed for each trim condition are then fed into the simulation as commanded inputs. Since the dynamics are nonlinear, there is no guarantee that the dynamic response will be stable; however, if the maneuver is performed slowly enough, excursions away from the trim points are minimized. The resulting trajectories for the perch and the pitch-up maneuvers are shown in Figure 2.14.

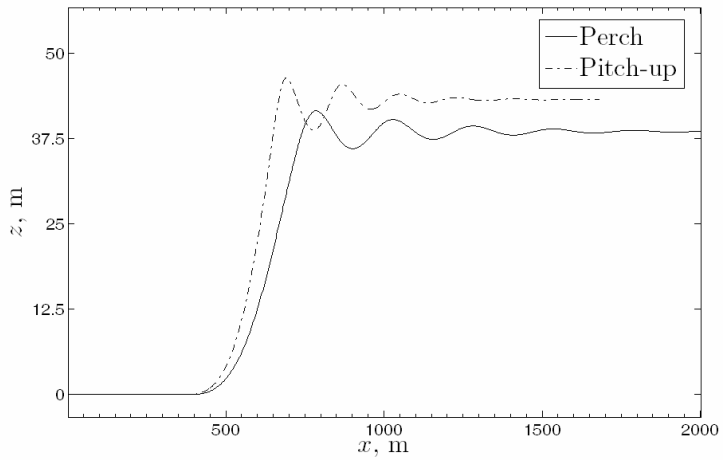

Figure 2.14: Open-loop position responses to commanded maneuvers

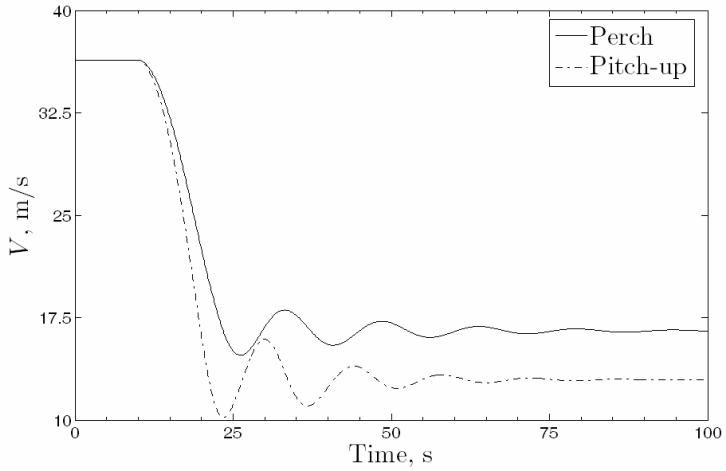

Figure 2.15: Open-loop velocity responses to commanded maneuvers

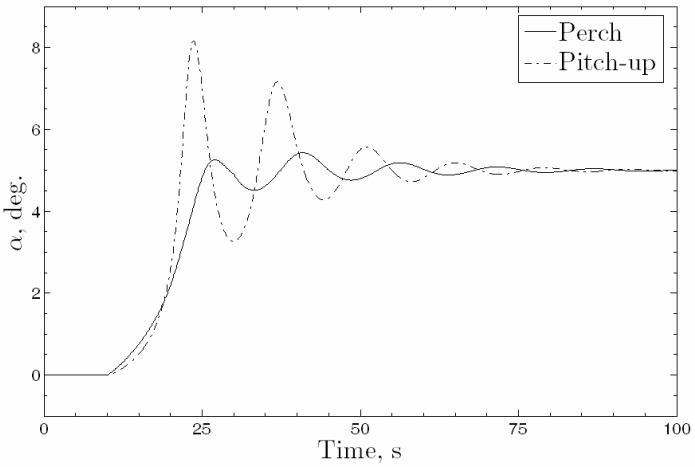

Figure 2.16 Open-loop angle of attack responses to commanded maneuvers

In these case, the maneuvers last from t = 10s until t = 30s. Note that these maneuvers produce stable responses with a relatively small change in steady-state altitude (compared to the distance traveled). Both the phugoid and short-period modes are excited, although only the phugoid mode is evident in Figures 2.14 – 2.16. The angle of attack reaches a peak at 5.5° for the perching maneuver and 8° for the pitch-up, with a steady-state value of 5° for both cases (thus returning the wings to a 0° angle of attack for the perching case). As depicted in Figure 2.12(b), both maneuvers reduce the trim velocity of the vehicle, with the pitch-up maneuver reducing it further. In addition, the pitch-up response is more highly damped; the only drawbacks are the increased overshoot in the transient response and the increased ruddervator deflection as discussed above.

5. Conclusion

The transient and steady-state behavior of a perching aircraft undergoing changes in flight condition and vehicle reconfiguration is discussed. This aircraft's unique morphology – consisting of variable wing incidence, tail boom angle, and tail incidence – is presented and shown to be effective for the initiation of a perching maneuver. The perching shape reconfiguration and a simple pitch-up are compared at low angles of attack using analytical and empirical methods. Whereas the pitch-up maneuver permits a similar reduction in air speed, vehicle reconfiguration avoids large steady-state deflections of the longitudinal control surfaces. Simulations also show that, although the pitch-up is more highly damped, its transient behavior brings the aircraft closer to instability at high angles of attack. Although simulation at low angles of attack does not suggest any new capabilities enabled by shape reconfiguration, at post-stall angles of attack, reconfiguration will be necessary to trim the aircraft, since attached flow will still be present over the wings and tail surfaces.

REFERENCES

[1] Sanders, B., Crowe, R., and Garcia, E., "Defense Advanced Research Projects Agency: Smart Materials and Structures Demonstration Program Overview," *Journal of Intelligent Material Systems and Structures*, Vol. 15, No. 4, 2004, pp. 227–233.

[2] Bowman, J., Sanders, B., and Weisshaar, T., "Evaluating the Impact of Morphing Technologies on Aircraft Performance," AIAA2002-1631, 2002.

[3] Wickenheiser, A., Garcia, E., and Waszak, M., "Evaluation of Bio-Inspired Morphing Concepts with Regard to Aircraft Dynamics and Performance," *Proceedings of SPIE: International Society for Optical Engineering*, Vol. 5390, 2004, pp. 202–211.

[4] Wickenheiser, A., Garcia, E., and Waszak, M., "Longitudinal Dynamics of a Perching Aircraft Concept," *Proceedings of SPIE: International Society for Optical Engineering*, Vol. 5764, 2005, pp. 192–202.

[5] Levine, J. S., Blaney, D. L., Connerney, J. E. P., Greeley, R., Head, J. W., Hoffman, J. H., Jakosky, B. M., McKay, C. P., Sotin, C., and Summers, M. E., "Science from a Mars Airplane: The Aerial Regional-Scale Environmental Survey (ARES) of Mars," AIAA2003-6576, 2003.

[6] Weissinger, J., "The Lift Distribution of Swept-Back Wings," NACA, TM-1120, 1947.

[7] DeYoung, J., and Harper, C. W., "Theoretical Symmetric Span Loading at Subsonic Speeds for Wings Having Arbitrary Plan Form," NACA, Report No. 921, 1948.

[8] Smith, S. C., Guynn, M. D., Streett, C. L., and Beeler, G. B., "Mars Airplane Airfoil Design with Application to ARES," AIAA2003-6607, 2003.

[9] McGranahan, B., and Selig, M., *UIUC Low-Speed Airfoil Tests*, URL: http://www.aae.uiuc.edu/m-selig/uiuc_lsat.html [cited 19 Feb. 2004].

[10] Schmidt, L., *Introduction to Aircraft Flight Dynamics*, AIAA Education Series, AIAA, Reston, VA, 1998, p. 113.

[11] Hoak, D. E., and Finck, R. D., "The USAF Stability and Control Datcom," Air Force Wright Aeronautical Lab., TR-83-3048, Oct. 1960 (Revised 1978).

[12] Zipfel, P., *Modeling and Simulation of Aerospace Vehicle Dynamics*, AIAA Education Series, AIAA, Reston, Virginia, 2000, p. 378.

[13] Qualls, G., *ARES: A Proposed Mars Scout Mission*, URL: http://marsairplane.larc.nasa.gov/multimedia.html [cited 10 Feb. 2004].

This chapter originally appeared as:

Wickenheiser, A., and Garcia, E. "Longitudinal Dynamics of a Perching Aircraft," *Journal of Aircraft*, Vol. 43, No. 6, 2006, pp. 1386-1392.

CHAPTER 3
OPTIMIZATION OF PERCHING MANEUVERS THROUGH VEHICLE MORPHING[1]

1. Abstract

Recent advances in UAV technologies have enabled new missions and flight capabilities for these aircraft. One such capability currently under investigation is perching, which involves the vertical landing of an aircraft using primarily aerodynamics as opposed to thrust generation. This chapter discusses the development and optimization of trajectories designed to bring a UAV from a loitering state to a planted landing. These trajectories are developed for attached, partially stalled, and fully stalled flow regimes. The effects of nonlinear aerodynamics and vehicle shape reconfiguration are shown to lessen the initial distance from the landing site required to initiate the maneuver, reduce the spatial bounds on the trajectory, and decrease the required thrust for the maneuver. The aerodynamics are modeled using empirical and analytical methods in both attached and separated flow regimes. Unsteady effects such as dynamic stall are also included in this model. Optimal solutions of varying thrust-to-weight ratio and center of gravity location are compared. Additionally, perching trajectories that compare morphing versus fixed-configuration and stalled versus un-stalled aircraft are presented in order to demonstrate the effects of relaxed constraints on vehicle geometry and flight envelope. Control effort is also evaluated in these simulations; specifically, the available control for disturbance rejection is compared for morphing versus fixed-configuration aircraft. The results of these comparisons show that morphing increases the controllability of the aircraft

[1] From Wickenheiser, A. and Garcia, E., "Optimization of Perching Maneuvers Through Vehicle Morphing"; reprinted by permission of the American Institute of Aeronautics and Astronautics, Inc.

throughout the maneuver as well as decreases the cost of the optimal perching trajectory.

2. Introduction

Lately, advances in smart materials, actuators, and control systems have enabled the development of new capabilities for aircraft [1]. Several studies have indicated that airframe reconfiguration can lead to increased flight performance and mission potential [2-4]. These studies have shown that in-flight vehicle morphing can grant a single aircraft increased performance by several typically incompatible metrics, such as endurance, turn radius, and dash speed. Lockheed Martin Skunkworks [5] and NextGen Aeronautics [6] have each produced flight-tested morphing UAV's that address the problem of adding dash capabilities to ISR (Intelligence, Surveillance, and Reconnaissance) platforms. The primary hurdle is that long endurance aircraft typically have high aspect ratio wings to increase lift-to-drag efficiency, whereas strike aircraft have shorter delta wings for improved high-speed flight. Both morphing UAVs utilize segmented folding wing mechanisms – the former, a gull-like wing, and the latter, a bat-like wing – in order to reduce the planform area and span of the wing drastically, thereby enabling high endurance and dash capabilities on a single airframe. In addition, new research has focused on developing bio-inspired flight capabilities for manmade aircraft, including flapping wing flight [7]. Another bio-inspired maneuver under development is perching. Perching can be described as a high angle-of-attack approach, with the purpose of using high-drag, separated flow for braking, followed by a planted landing [8-9]. While vertical landings are relatively straightforward for high thrust-to-weight aircraft, it has yet to be demonstrated for high efficiency reconnaissance platforms. For example, the perching capability could enable an ISR

mission length to be extended dramatically: once a target has been found, the aircraft may land on a nearby structure and continue to survey an area without consuming fuel for flight.

ISR aircraft generally do not feature high thrust or thrust vectoring; therefore, another mechanism for decelerating the vehicle must be exploited. In addition, the stall speed of low thrust aircraft is usually too high for landing on a small surface. Akin to soaring birds [10], a perching aircraft of low thrust-to-weight ratio must fly below the point of landing and then "pop up" just before touchdown, using gravity to drain away the last of its kinetic energy. While this undershoot is impossible on flat ground, it can be exploited for a short landing on an elevated platform. In an urban environment, this type of landing site is prevalent and is ideal for extended surveillance missions as previously mentioned. In order to generate the most rapid decrease in kinetic energy, flying in a stalled flow regime is desirable; however, this introduces stability and controllability problems since unsteady force amplitudes from the separated wake are high and the effectiveness of control surfaces is greatly diminished.

Aerodynamic perching has been studied before in the form of stalled landings [11]; however, the controllability of a typical low-thrust aircraft in a deep stall is questionable, and the large undershoot of the trajectory relative to the landing site is undesirable. It is proposed that in-flight shape reconfiguration will be able to allay both of these concerns. The particular aircraft used to develop the perching maneuver is based on the Aerial Regional-Scale Environmental Survey (ARES) Mars scout craft, an aircraft designed to unfold from a Viking derivative aeroshell and fly for approximately 81 minutes over a Martian landscape, collecting data on atmospheric chemistry, geology, and crustal magnetism [12]. The complete details of the perching

aircraft's capabilities are described in Ref. 9; however, the prominent features are depicted in Figure 3.1. Unlike the original ARES or any conventional aircraft, additional degrees of freedom are incorporated into the tail boom and tail incidence, and variable incidence is added to the wing sections (or outboard sections of the blended wing body). These degrees of freedom allow the aircraft to change shape in flight, thus grossly altering the geometry and the aerodynamics of the aircraft.

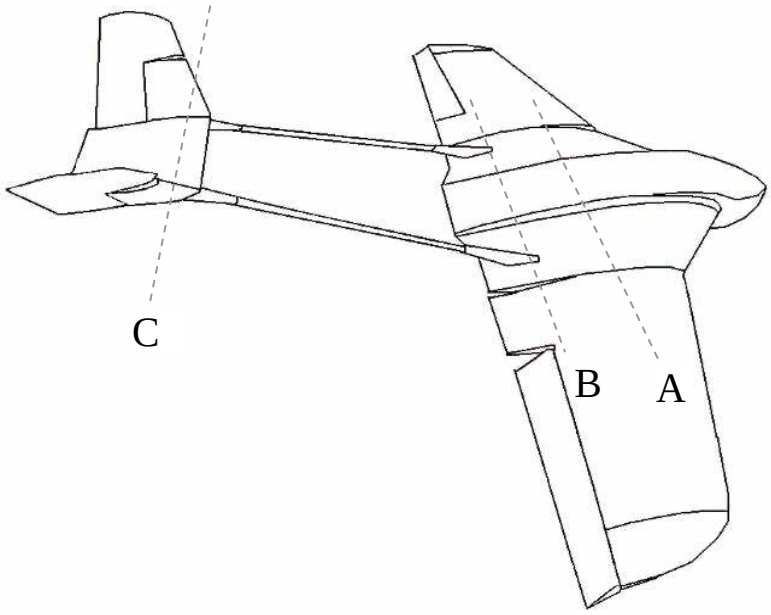

Figure 3.1: The three shape-change actuations about the pitch axis: A) rotation of the wing incidence angle with respect to the fuselage body axis, B) rotation of the tail boom, and C) rotation of the horizontal stabilizer

The principal reasoning behind these additional degrees of freedom is to create regions of attached and separated flow over the aircraft through various flight regimes. As will be demonstrated, high-drag, separated flows are necessary to produce practical perching maneuvers. However, it is also desired to maintain controllability about the aircraft's axes of rotation, for which attached flow over the control surfaces is necessary. Thus, while the fuselage (or inboard section of the blended wing body) is

pitched up to high incidence, the wings are rotated down to maintain attached flow over the ailerons. Additionally, the tail is rotated down and out of the resulting unsteady wake of the body, and the horizontal stabilizer is also actuated in order to keep the tail surface horizontal as the tail boom rotates. This morphological change keeps the standard aileron and ruddervator surfaces effective at trimming and control. They also allow a larger degree of control over the aircraft's dynamics through a wider range of flight conditions.

The "direct shooting method" [13] of solving optimization problems is used to convert the nonlinear optimization problem into an equivalent nonlinear programming problem. This procedure involves converting the control time histories into a simple functional form that can be parameterized by a (relatively) small number of constants. Several parameterizations have been tested before selecting a piecewise cubic Hermite interpolation. This method of interpolation can be designed to preserve the monotonicity and extrema of the underlying data [14], as well as providing continuity and continuous differentiability of the time series. This is especially significant since the optimal control strategies tend to be only piecewise continuous due to constraints, which might be violated by any overshoot in the interpolating polynomial. The optimization method used in this study is a combination of simulated annealing [15] and sequential quadratic programming [16]. These methods are used in conjunction in order to balance robustness against local minima and speed of convergence. Several methods for discretizing and numerically integrating the dynamics have been considered; however, Matlab's 4th-5th order adaptive Runge-Kutta algorithm [17] has been chosen for its robustness in the face of fast dynamics (i.e. pitch dynamics) coupled with slow dynamics (i.e. translational dynamics).

In this chapter, the perching trajectory optimization problem is rigorously formulated to provide a framework for generating practical maneuvers for the reconnaissance mission previously described. The governing dynamics of the aircraft and the surrounding flow are presented, as well as the physical and heuristic constraints placed on the solution. Results of the optimization procedure are presented for several classes of aircraft models, including point-mass, fixed-configuration, and morphing airframes. Finally, several conclusions are offered about the important parameters in this problem and about the variations in optimal solutions among these classes.

3. Problem Formulation

The trajectory optimization problem is formulated as a two-point boundary value problem between a cruising state and a perching state (zero velocity) at a specified point. The final state is further restricted to have a pitch angle between 0-90 deg so that the aircraft perches on its landing struts. All of the aircraft controls (standard and morphing) are limited in range and actuation rate, as summarized in Table 3.1. (The layout of these controls is depicted in Ref. 8 and Figure 3.2) The lower bound on the tail boom angle is set at -15 deg in order to keep it out of the unsteady wake behind the fuselage at high angles of attack. Although it is assumed that the throttle setting is not rate limited, every optimal control strategy indicates that the throttle should be at maximum throughout most of the maneuver, as will be shown. For this study, the thrust vector is assumed to be aligned with the chord line of the fuselage. The nominal values listed in Table 3.1 correspond to the cruise configuration of the aircraft.

Table 3.1: Actuator Constraints

		Nominal value, deg	Range, deg	Maximum Rate, deg/s
ι	wing incidence angle	0	-90 – 90	±20
θ_b	tail boom angle	-15	-15 – 90	±20
θ_t	tail incidence angle	-15	-90 – 90	±20
δ_e	elevator angle	0	-20 – 20	±40

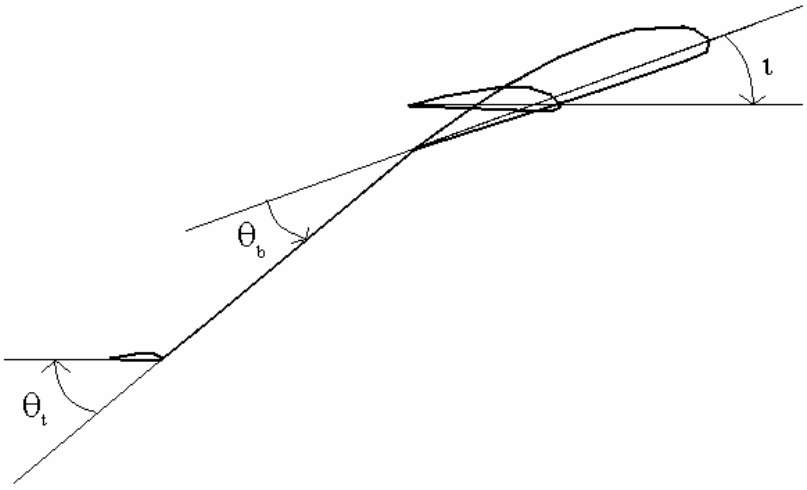

Figure 3.2: Morphing parameters, with directions of increasing value

In order to maximize the convergence rate and minimize any numerical errors from poor scaling [18], the longitudinal equations of motion are converted into the following nondimensional form:

$$\dot{V} = T\cos\alpha - C_D V^2 - \sin\gamma \tag{1}$$

$$\dot{\gamma} = \frac{T}{V}\sin\alpha + C_L V - \frac{\cos\gamma}{V} \tag{2}$$

$$\dot{q} = \kappa C_M V^2, \quad \kappa = \frac{2\bar{c}m^2}{\rho S I_Y} \tag{3}$$

$$\dot{\theta} = q \tag{4}$$

$$\dot{x} = V\cos\gamma \tag{5}$$

$$\dot{h} = V \sin\gamma \tag{6}$$

$$\alpha = \theta - \gamma \tag{7}$$

where V is in units of $\sqrt{gl}$, t is in units of $\sqrt{g/l}$, T is in units of mg, and x and h are in units of l, where $l = 2m/\rho S$ is the characteristic length. With angles measured in radians, all of the aircraft's states are now of order one.

A cost function is chosen to minimize the spatial bounds of the trajectory. With a thrust-to-weight ratio less than one, the trajectory invariably "undershoots" the landing site, since an increase in potential energy is required to reduce the speed to zero. Thus, the cost function addresses two major concerns: minimizing the undershoot and minimizing the distance from the landing site required to start the maneuver. Both goals have great practical value. Minimizing the undershoot is important due to spatial limitations, since the landing site may be close to or at ground level. Minimizing the required distance to start the maneuver is important because on-board sensors have a finite range at which they can identify and track the landing site. Figure 3.3 depicts several perching trajectories for conventional aircraft with varying constraints on the maximum angle of attack. The initial state is the aircraft's straight and level trim point for maximum endurance, and the final state is zero velocity at the origin.

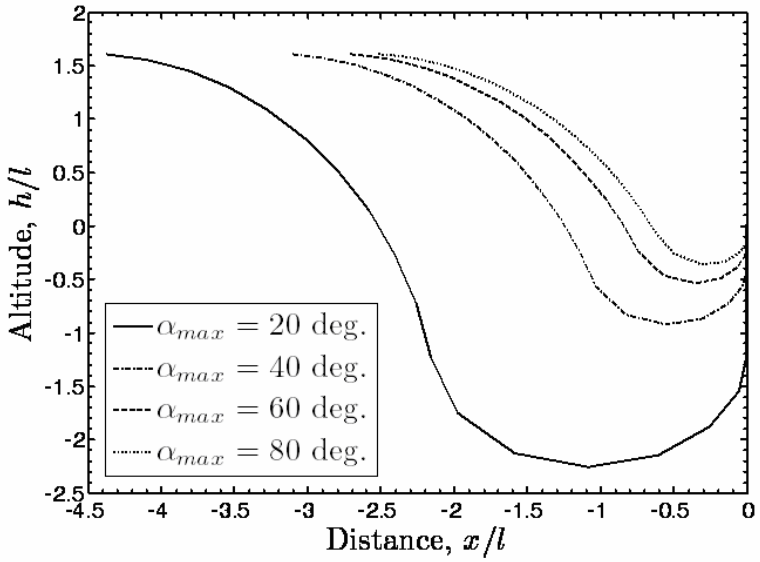

Figure 3.3: Perching trajectories for a conventional aircraft of varying maximum angle of attack ($T/W_{max} = 0.1$)

These results confirm the persistent undershoot in the trajectories, as well as motivate the division of the problem into two halves. For this study, the goal of minimizing undershoot is given higher priority; thus, the problem can be divided and solved sequentially [19]. These two halves, called the dive phase and the climb phase, are depicted in Figure 3.4.

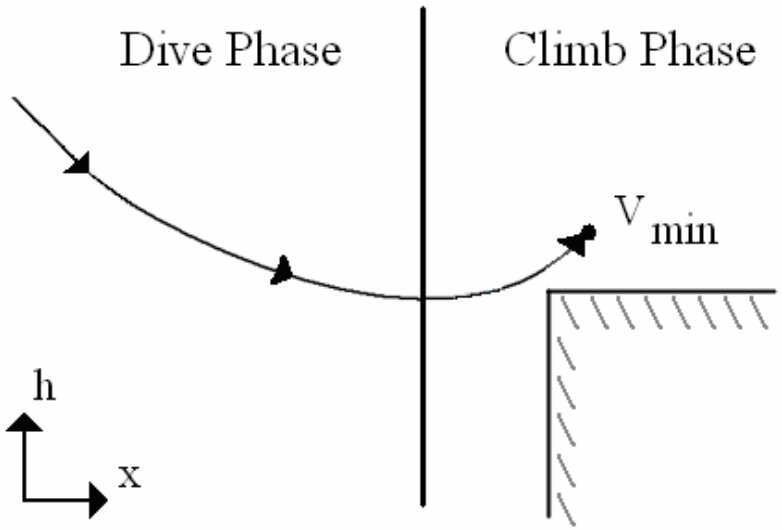

Figure 3.4: Division of the perching trajectory optimization problem into two phases

The climb phase can be solved first for minimum undershoot by integrating the equations of motion (Eqs. (1-7)) from the lowest point of the trajectory (where $\gamma = 0$ deg) to the landing site. The final velocity is specified, and the goal is to minimize the change in height between the initial and final points of the trajectory. The global (over all possible trajectories) minimum undershoot is a function only of the climb phase since only the dynamics here determine how quickly the aircraft can pull up to the landing site with the specified final speed. This proposition assumes that the initial condition of the climb phase is a reachable end condition of the dive phase. The dive phase then connects the initial condition to the starting point of the climb phase. The objective of this phase is to minimize the starting distance – which could be specified as horizontal, vertical, or Euclidean, for example – required to attain a final condition that matches the initial condition of the climb phase. Thus, the cost functions for the two phases can be written as

$$J_{\text{dive}} = x_f \text{ or } h_f \text{ or } \sqrt{x_f^2 + h_f^2} \tag{8}$$

$$J_{\text{climb}} = -\min_{t \in [t_0, t_f]} h(t) \tag{9}$$

The requirement to minimize maximum undershoot (Eq. (9)) determines the optimal trajectory for the climb phase, which in turn determines the end condition of the dive phase. Thus, the optimal solution for the dive phase is only optimal among the set of trajectories that match up with the optimal trajectory for the climb phase. Although the solution to the dive phase may be suboptimal over all possible trajectories, it is optimal given the constraint that minimizing the maximum undershoot is the highest priority.

For the purposes of this study, the aircraft is modeled in the longitudinal plane only; that is, roll, yaw, and sideslip dynamics are not considered. This assumption simplifies the aerodynamics and vehicle dynamics substantially while still providing an environment for studying the richness and qualitative behavior of the perching maneuver. The aerodynamic forces on the aircraft components in the attached flow regime are calculated using a modified version of Weissinger's method [20], as developed by Wickenheiser and Garcia [21]. This method has been developed with morphing aircraft in mind; hence, thousands of aircraft configurations have been able to be computed in a matter of days. This process has produced a lookup table of aerodynamics to be used for simulation in the attached flow regime.

Since experimental data of this particular aircraft at high angles of attack are not yet available, flat-plate assumptions and preexisting high angle of attack data [22] have been used where the flow is separated. These assumptions are not unreasonable since

specific airfoil shape becomes less significant after the flow has detached. The aerodynamic model for fully separated flow is summarized in the following equations:

$$C_{L,sep} = 1.1\sin(2\alpha) \tag{10}$$

$$C_{D,sep} = .9(1-\cos(2\alpha)) \tag{11}$$

$$\left(\frac{x_{cp}}{c}\right)_{sep} = .04095\alpha + .0857 \tag{12}$$

where the center of pressure in Eq. (12) is measured aft of the quarter-chord point. Furthermore, a mixing parameter p is introduced to handle the nonlinear transition between attached and separated aerodynamics and to account for dynamic stall effects. This term is modeled as a first-order lag state, as recommended by Goman and Khrabrov [23], subject to the dynamics of Eq. (13),

$$\tau_1 \dot{p} = p_0(\alpha - \tau_2 \dot{\alpha}) - p \tag{13}$$

where p_0 is the steady-state mixing function given by

$$p_0(\alpha) = \begin{cases} 1 & |\alpha| < 4^\circ \\ -.3326\tan^{-1}\left(\frac{180}{\pi}|\alpha| - 16\right) + .5 & 4^\circ \le |\alpha| \le 37^\circ \\ 0 & |\alpha| > 37^\circ \end{cases} \tag{14}$$

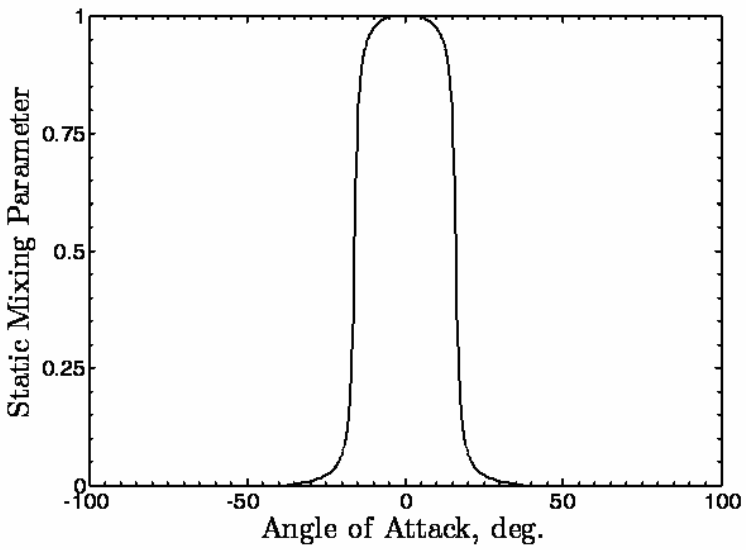

Figure 3.5 Static mixing parameter p_0

Thus, as evinced by Eq. (14) and Figure 3.5, $p = 1$ corresponds to fully attached flow and $p = 0$ corresponds to fully separated flow, with values in between indicating partially separated flows. The model for the mixing parameter given by Eqs. (13-14) realistically accounts for static and dynamic stall effects. The $(\alpha - \tau_2 \dot{\alpha})$ term accounts for time delays in flow separation and reattachment caused by boundary-layer convection lag, which is roughly proportional to $\dot{\alpha}$. The $\tau_1 \dot{p}$ term accounts for the transient response of the flow to disturbances; this is simply modeled as a first-order dynamical system. Both time constants $\tau_{1,2}$ scale with the characteristic time scale $(\bar{c}/V)$. By utilizing the mixing parameter, the lift coefficient for any angle of attack is given by

$$C_L(\alpha, \dot{\alpha}) = C_{L,att}(\alpha) \cdot p(\alpha, \dot{\alpha}) + C_{L,sep}(\alpha) \cdot (1 - p(\alpha, \dot{\alpha})) \tag{15}$$

where it is clear that the total force is the weighted sum of the contributions from attached and separated flows. Similar expressions can be written for the drag and pitching moment coefficients. Since the wing and tail incidences can be varied with

respect to the fuselage angle of attack, separate states are required to model the degree of separation over each of these surfaces. Thus, the full state vector is

$$\mathbf{x} = \begin{bmatrix} V & \gamma & q & \theta & x & h & p_{fuse} & p_{wing} & p_{tail} \end{bmatrix}^{\mathbf{T}} \tag{16}$$

concatenating states from the equations of motion (Eqs. (1-6)) and the equation of flow separation (Eq. (13)).

In Figure 3.6, static C_L and C_M are plotted versus angle of attack for several values of elevator deflection. In the attached flow region, C_L and C_M are approximately linear, and the negative C_M slope indicates static pitch stability. At stall, lift decreases rapidly over the aircraft, and the restoring moments begin to level out. This means that less control effort is required to pitch the aircraft further than if the flow had remained attached at all angles. In the next section, the relationship between stability and control effort in the perching maneuver is discussed in detail, especially with regards to the cost being optimized. Figure 3.7 depicts the dynamic stall phenomenon during rapid change of angle of attack. As shown, rapid change in angle of attack causes separation and reattachment to be delayed, as governed by Eq. (13). The combination of the nonlinear static aerodynamics and the dynamic stall effects constitutes the aerodynamic model used throughout this study.

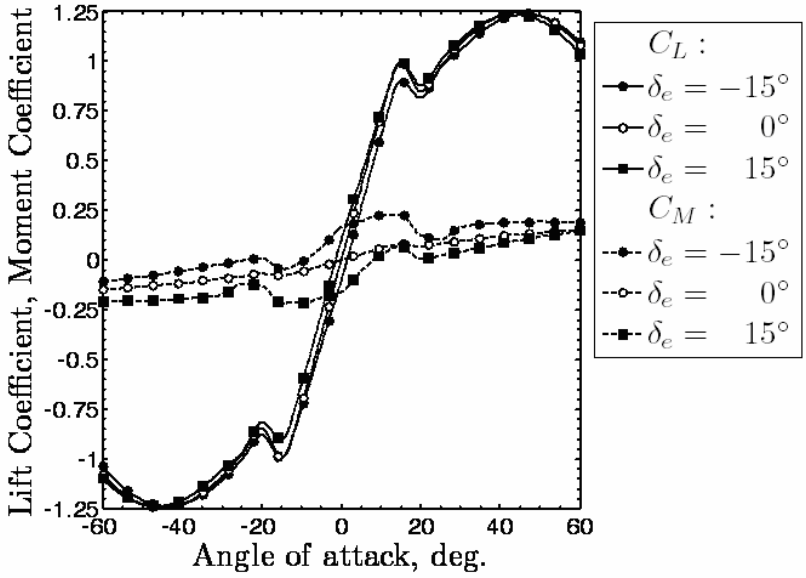

Figure 3.6: Lift and Moment Coefficients for several elevator deflections

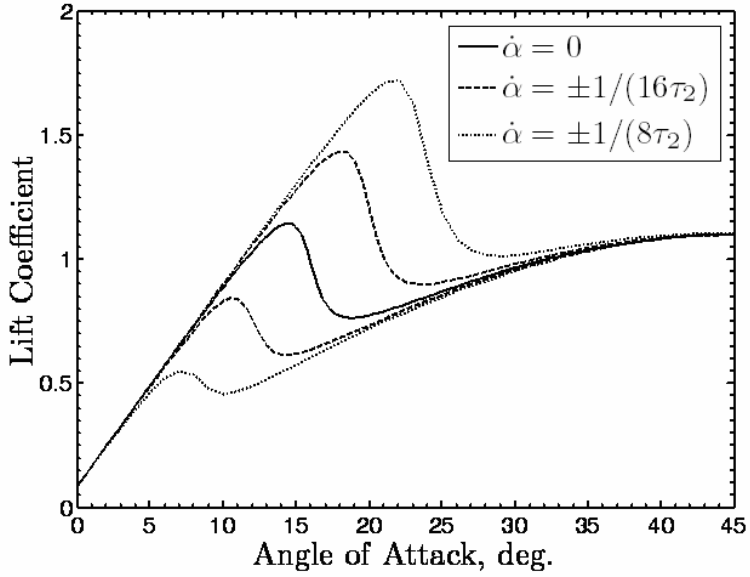

Figure 3.7: Dynamic stall due to rapid angle of attack changes

4. Optimization Results

4.1 Point-mass Aircraft

Before studying the complete nonlinear, morphing model of the aircraft, several simplifications are made in order to understand the perching trajectory optimization problem fully. The first simplification is to remove the pitch dynamics from the problem. Hence, the aircraft becomes a point mass moving along its trajectory with a variable angle of attack (a control parameter) that determines the lift and drag forces on the aircraft. This enables the trajectory to be optimized without regard to the pitch dynamics, which tend to occur on a much faster time scale than the translational dynamics. This simplifies the optimization and provides an estimate of the optimal trajectory in the limit of infinitely fast pitch dynamics.

The effects of varying the allowable final velocity are studied initially, since intuitively this will have a great impact on the maximum undershoot of the trajectory. Since the speed of the aircraft is very slow throughout the final part of the climb phase, gravity, as opposed to drag, is the primary means by which the kinetic energy of the aircraft is reduced. By allowing a larger final kinetic energy, less change in gravitational potential is required for energy conversion. If the final velocity must be zero, then the aircraft must be flying vertically at the end of the trajectory since the aerodynamic forces must go to zero as well. This is undesirable since it requires the aircraft to fly very close to the structure upon which it is landing. Conversely, if the final velocity is permitted to be greater than zero, then the final approach will be horizontal for minimum undershoot. This can be seen in Figure 3.8, where trajectories of different initial kinetic energy (i.e. velocity) are plotted.

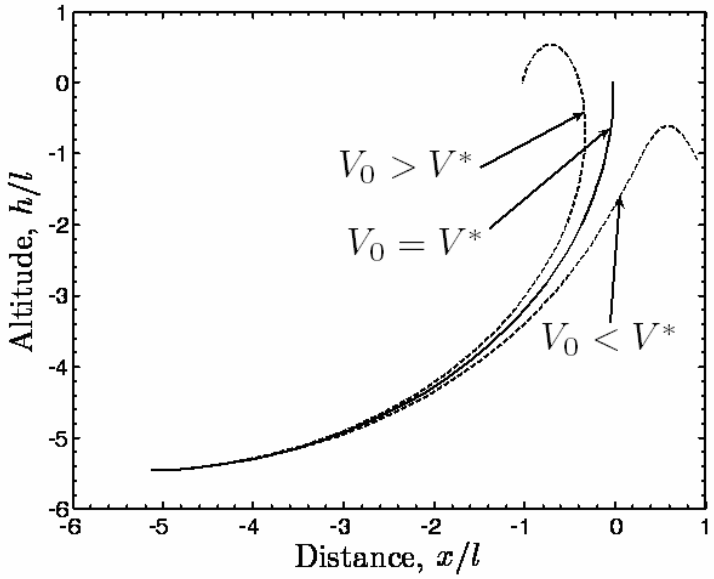

Figure 3.8: Climb phase trajectories of varying initial velocity

In Figure 3.8, V^* is the initial velocity required to reach $V = 0$ at $(x,h) = (0,0)$ from the given starting position. This trajectory is sensitive in the meaning that a small perturbation in initial velocity causes a qualitative change in the resultant trajectory. As shown, a greater velocity causes the aircraft to overshoot the landing site and loop back on itself, whereas a lesser velocity causes it to stall before it reaches $V = 0$ and then dive again. In all three cases, the minimum velocity occurs at the peak of the trajectory. If the required final velocity is allowed to be greater than zero, then the lower trajectory ($V_0 < V^*$) can be shifted upward until the peak is at (0,0); thus, the undershoot will be less than the $V_0 = V^*$ trajectory. It is therefore apparent from these simple simulations that increasing the allowable landing speed must decrease the maximum undershoot.

Next, the effects of varying the maximum angle of attack and maximum thrust-to-weight ratio are studied. Both of these parameters are important design parameters because they determine the engine size and the extent of morphing required in order to keep the wings at a low angle of attack. Based on the equations of motion (Eqs. (1-6)), the optimal trajectory should feature high lift during the initial part of the climb phase (when $\dot{\gamma}$ is positive), and high drag at the very end (when $\dot{V}$ is negative). This is indeed the case, as shown in Figures 3.9 – 3.10. Comparing the prescribed angles of attack in Figure 3.10 with the aerodynamics in Figure 3.6 indicates that initially the aircraft is pitched to the angle of attack for high lift and high drag and then progresses to the angle of attack for maximum drag. In most cases this means landing at the maximum angle of attack. The α_{max} = 20 deg case is different because its aerodynamics are dominated by an angle of attack range over which the lift coefficient is not monotonically increasing with α: its maximum angle of attack has relatively low lift. Indeed, the optimal control hovers around the stall point (α = 15 deg), where both lift and drag are high. Higher angles of attack would result in a loss of lift that would prevent the aircraft from reaching the peak of its trajectory with minimum undershoot. Figure 3.10 also indicates that the aircraft that are restricted to lower angles of attack take longer to complete the maneuver. This reflects the fact that these aircraft cannot produce as high drag for deceleration.

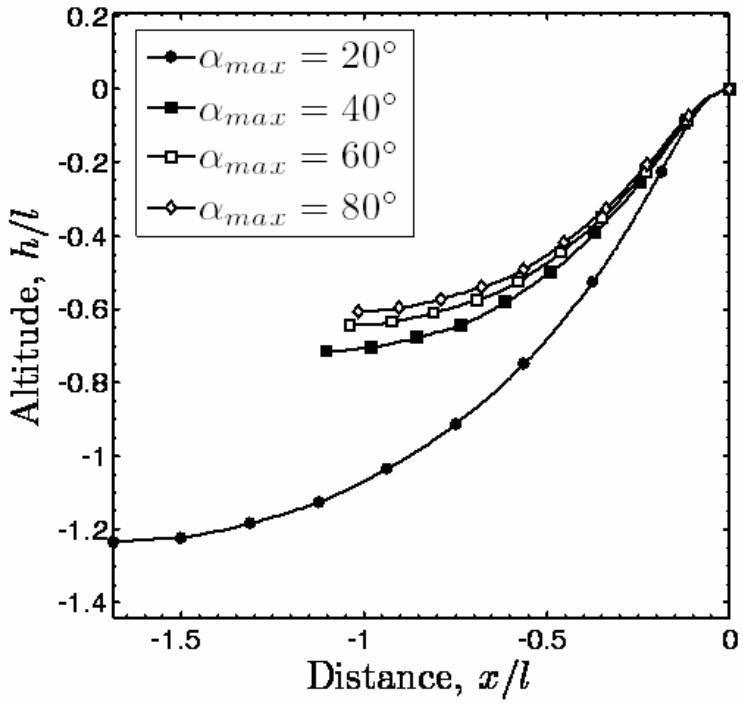

Figure 3.9: Point-mass aircraft climb phase trajectories of varying maximum angle of attack ($T/W_{max} = 0.1$)

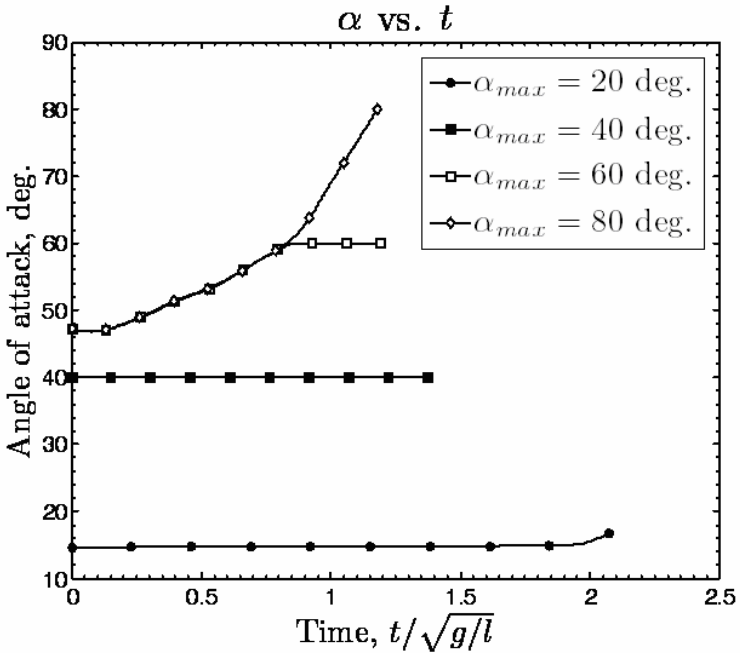

Figure 3.10: Angle of attack vs. time for point-mass aircraft climb phase trajectories of varying maximum angle of attack ($T/W_{max} = 0.1$)

The variations with respect to thrust-to-weight ratio, with maximum angle of attack held constant, are depicted in Figures 3.11 – 3.12. As expected, a higher thrust-to-weight ratio permits lower undershoot. Physically, this seems counterintuitive – after all, the objective is to minimize the kinetic energy of the system, whereas thrust can only increase it – but additional thrust allows the aircraft to fly at a slower speed while still climbing, since the thrust line is not aligned with the velocity vector at nonzero angles of attack. Figure 3.12 indicates that maximum thrust is applied throughout the maneuver, and it is only throttled right before landing. This throttling causes the aircraft to pitch down so that its final velocity is purely horizontal.

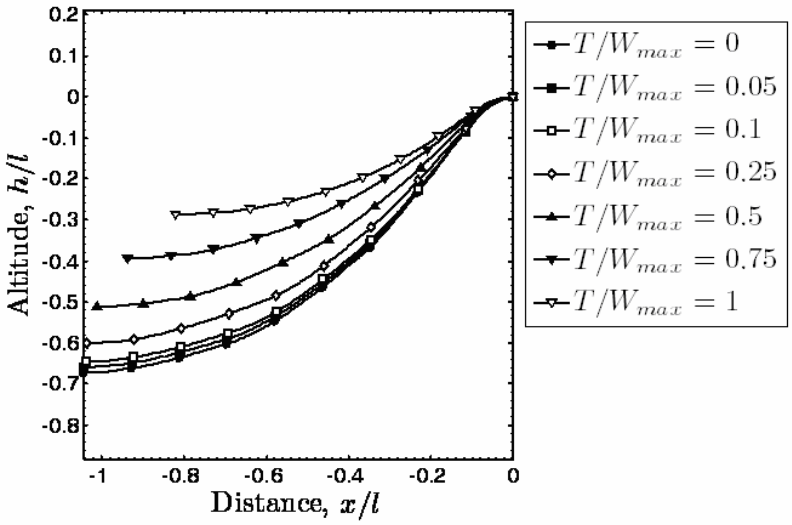

Figure 3.11: Point-mass aircraft climb phase trajectories of varying maximum thrust-to-weight ratio (α_{max} = 60°)

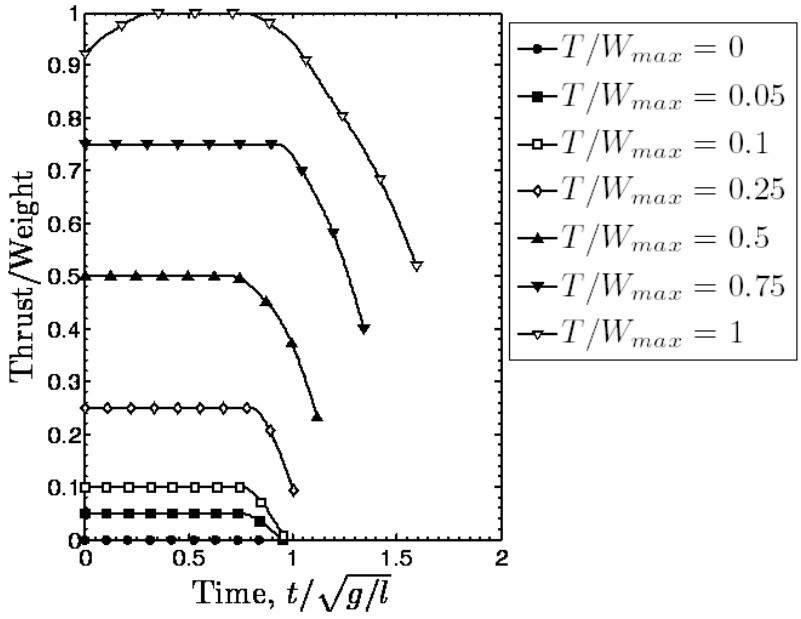

Figure 3.12: Thrust-to-weight ratios vs. time for point-mass aircraft climb phase trajectories of varying maximum thrust-to-weight ratio (α_{max} = 60°)

Complete trajectories of various maximum thrust-to-weight ratios are shown in Figure 3.13. The dive phase for each variation is adjoined to its corresponding climb phase, with the end of each climb phase set to (0,0). For each thrust-to-weight ratio, the dive phase is optimized for minimum altitude necessary to reach the required velocity at the start of the climb phase. For ratios greater than 0.25, this altitude is zero (with respect to the start of the climb phase), since with this much available thrust the aircraft can trim at the required velocity for the climb. Below 0.25, diving is required to gain the kinetic energy needed to start the climb. It is assumed that the aircraft speeds up to its maximum trim velocity before diving, so there is an acceleration phase that occurs before the dive phase that is not depicted in Figure 3.13.

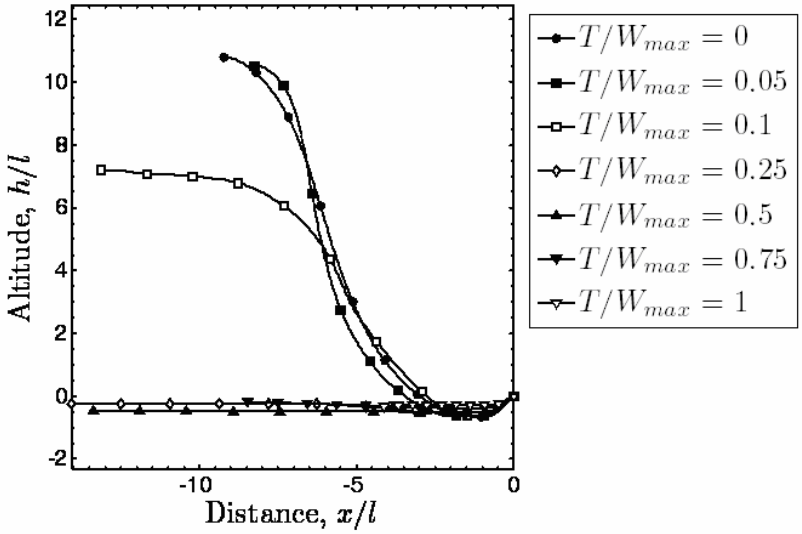

Figure 3.13: Point-mass aircraft full trajectories of varying maximum thrust-to-weight ratio ($\alpha_{\max} = 60°$)

4.2 Conventional Aircraft

Although the point-mass aircraft problem provides an adequate picture of the qualitative behavior of the perching problem, the bounds of the computed trajectories (i.e. the undershoot and the starting distance) are unrealistically small. This is due to the fact that the aircraft can pitch as fast as is needed to optimize the trajectory, without regard to rotational inertia or actuator limits. With the addition of the pitch dynamics governed by Eqs. (3-4), the pitch rate is now limited by the maximum achievable pitch moment and scaled by the rotational inertia of the aircraft. The pitch moment coefficient C_M in Eq. (3) is a function of the aircraft's angle of attack and the state of its geometry as determined by the actuators listed in Table 3.1. There is an additional pitch damping term C_{M_q}, proportional to the pitch rate q, that effectively smoothes out rapid changes in pitch angle. While this is desirable for gust alleviation,

it is undesirable for maneuvers since the aircraft must produce a greater pitch moment from its control surfaces in order to achieve rapid changes in pitch.

The effects of the pitch dynamics can be seen by comparing the trajectories in Figures 3.11 and 3.13 with Figures 3.14 – 3.15. As predicted, the trajectories bear the same qualitative shape with much larger spatial bounds. Since the aircraft cannot pitch up as rapidly, it requires more distance in which to complete the climb phase. In Figures 3.16 – 3.17, maximum thrust-to-weight ratio is held constant, whereas the center of gravity position is varied with respect to the aircraft's neutral point. These plots indicate that the unstable aircraft ($x_{cp} = x_{np} - \bar{c}$) has a lower-cost (i.e. smaller spatially) optimal trajectory than the neutrally stable and stable aircraft. Since the unstable aircraft can pitch faster with less elevator deflection, the aircraft is able to fly slower and still climb in order to complete the maneuver. The lower flight speed requirement translates directly into smaller spatial bounds of the trajectory. Thus, the aircraft's relative pitch stability plays a major role in its perching capability.

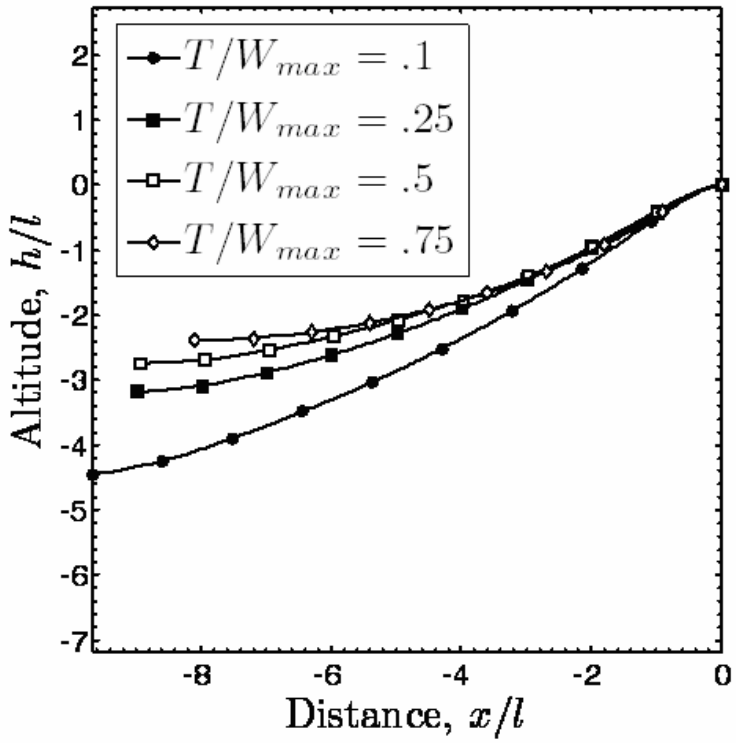

Figure 3.14: Climb phase trajectories of varying maximum thrust-to-weight ratio

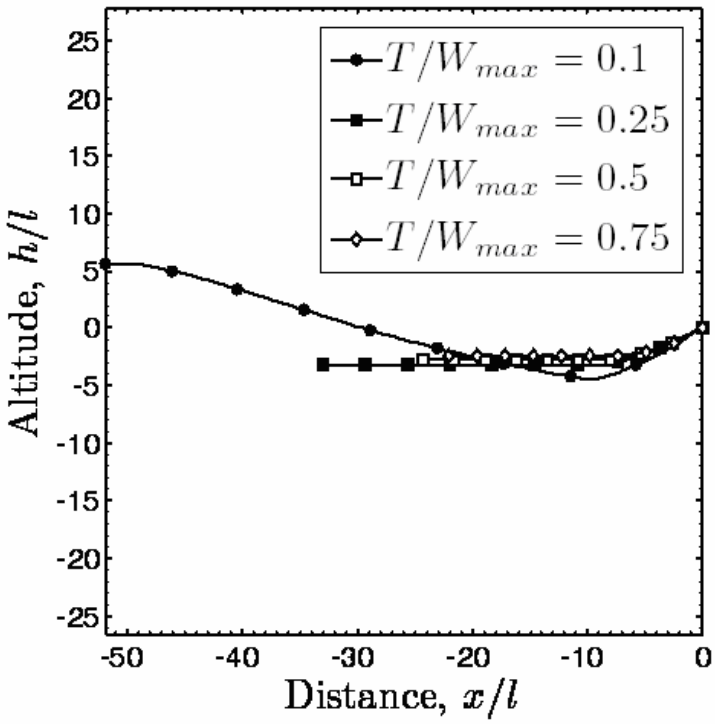

Figure 3.15: Full trajectories of varying maximum thrust-to-weight ratio

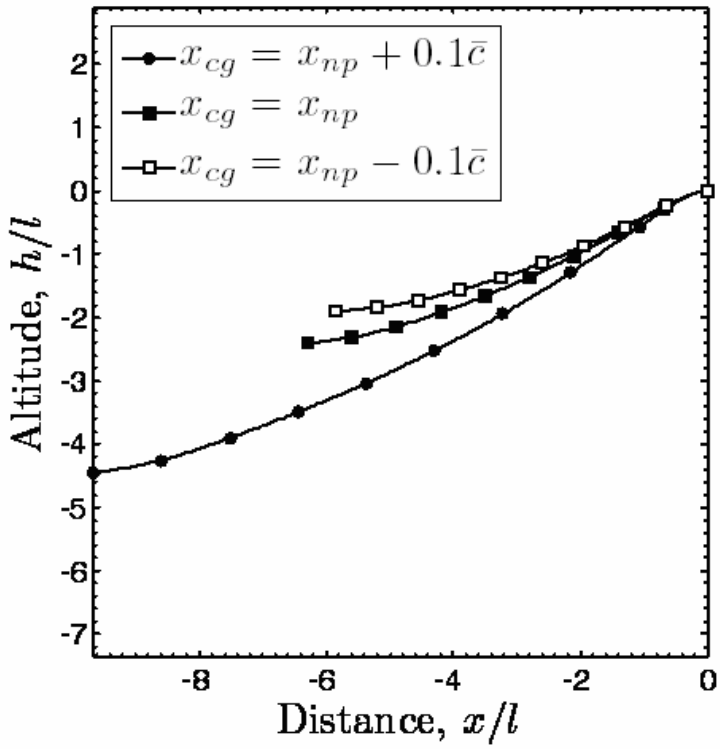

Figure 3.16: Climb phase trajectories of varying center of gravity location (T/W_{max} = 0.1)

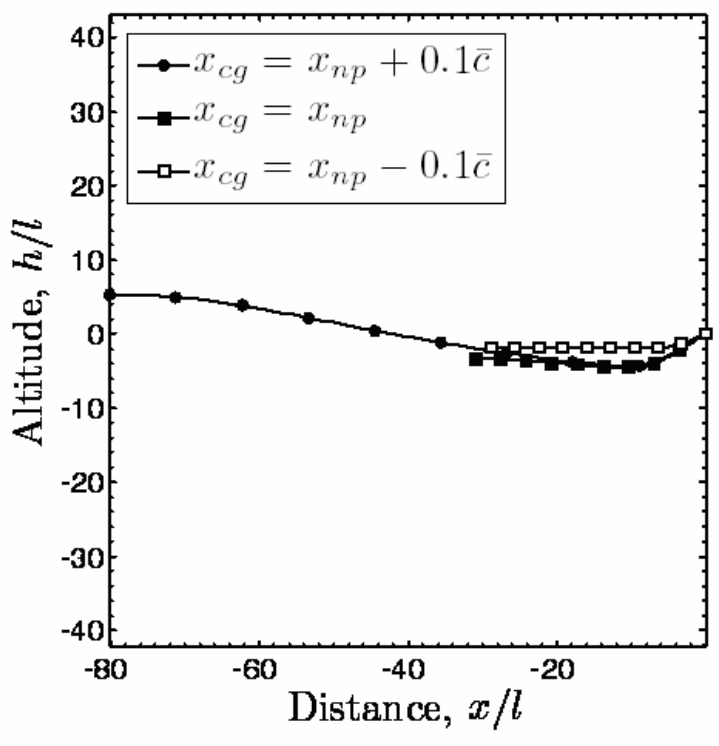

Figure 3.17: Full trajectories of varying center of gravity location (T/W_{max} = 0.1)

4.3 Morphing Aircraft

In-flight morphing allows the aircraft's dynamics to approach the point-mass case much more closely by enabling much larger possible pitching moments. This is because the morphing actuator ranges are much larger than the elevator's, as listed in Table 3.1; therefore, the lifting surfaces are able to rotate to higher angles of attack in order to generate larger pitching moments. By comparing the climb phase trajectories in Figures 3.16 and 3.18, the direct results of these greater pitching moments can be seen by noting the reduced undershoot in the morphing case. Figure 3.19 depicts the time histories of the morphing parameters for the climb phase. In these simulations the elevator deflection is held at zero to isolate the effects of vehicle reconfiguration.

The wing incidence time history indicates that the wings should be pitched down as the fuselage pitches up, thereby maintaining attached flow over the wings throughout the maneuver. This is beneficial for maintaining aileron effectiveness and for maximizing the pitching moment contribution of the wings. Since, for the morphing aircraft, the wings are not generating a large moment due to drag, their position with respect to the center of gravity is less significant compared to the tail's position. Thus, the morphing aircraft is less sensitive to changes in the center of gravity location compared to the fixed-configuration case of the previous subsection, as seen by comparing Figures 3.16 and 3.18. The tail boom remains fixed at its lower bound, which produces the largest moments due to down force and drag on the tail. The tail incidence angle is gradually increased throughout the maneuver, thereby producing a greater and greater negative tail angle of attack. At first, this produces a large down force on the tail, pitching the aircraft up. As the aircraft approaches the landing site, the angle of attack decreases further, thereby increasing the drag and slowing and pitching down the aircraft. Figures 3.20 – 3.21 describe full trajectories of the morphing aircraft with varying thrust-to-weight ratios. For the dive phase, the aircraft must morph from its cruise configuration to the configuration in which it begins the climb phase over the shortest distance. As shown, additional thrust enables the aircraft to fly at much lower speeds, thus shortening this distance. The wing incidence and tail incidence increase monotonically over this phase, indicating a transition from one trim state at cruise to another at the bottom of the trajectory. The tail boom is swung down and then back up again, which serves to pitch the aircraft down in order to gain speed for the climb phase. Figure 3.22 presents a direct comparison between a fixed-configuration and a morphing aircraft of the same thrust-to-weight ratio, indicating the orientation of the aircraft at several points along the trajectory. It is apparent that

morphing helps increase the maneuverability of the aircraft, thus enabling it to perch within a much shorter distance.

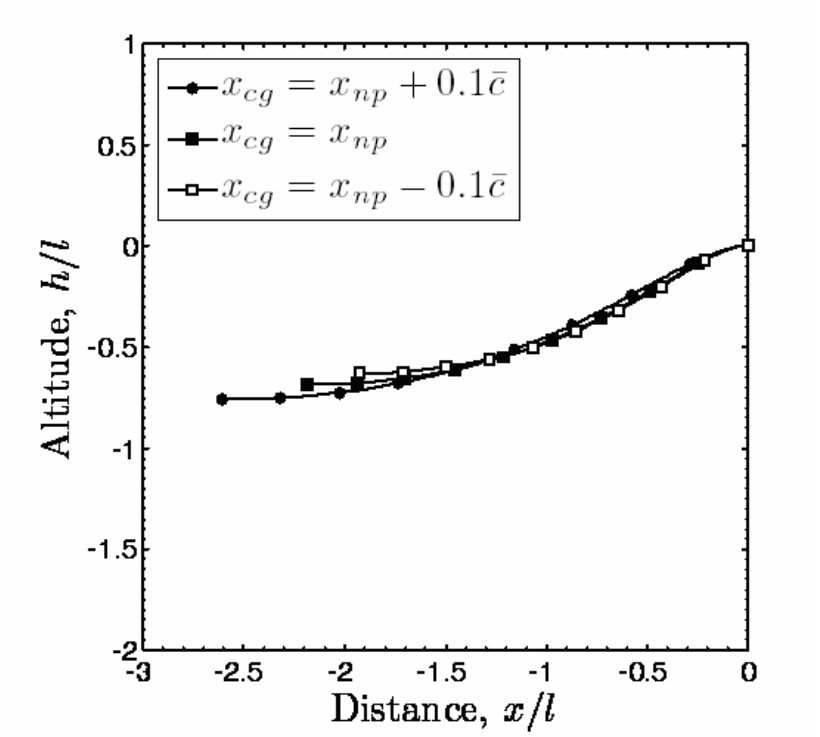

Figure 3.18: Climb phase trajectories of varying center of gravity location for the aircraft with morphing (T/W_{max} = 0.1)

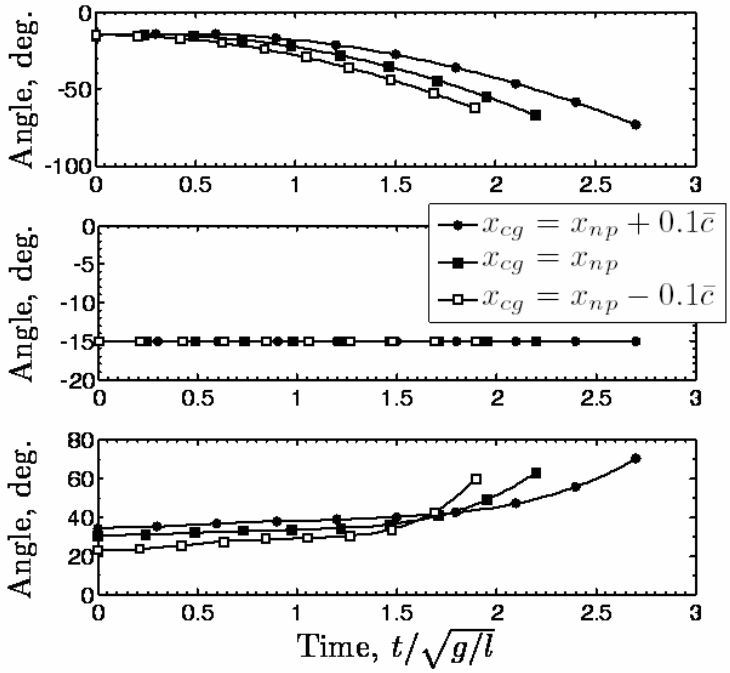

Figure 3.19: Climb phase morphing parameter time histories of varying center of gravity (T/W_{max} = 0.1): wing incidence (top), tail boom angle (middle), and tail incidence (bottom)

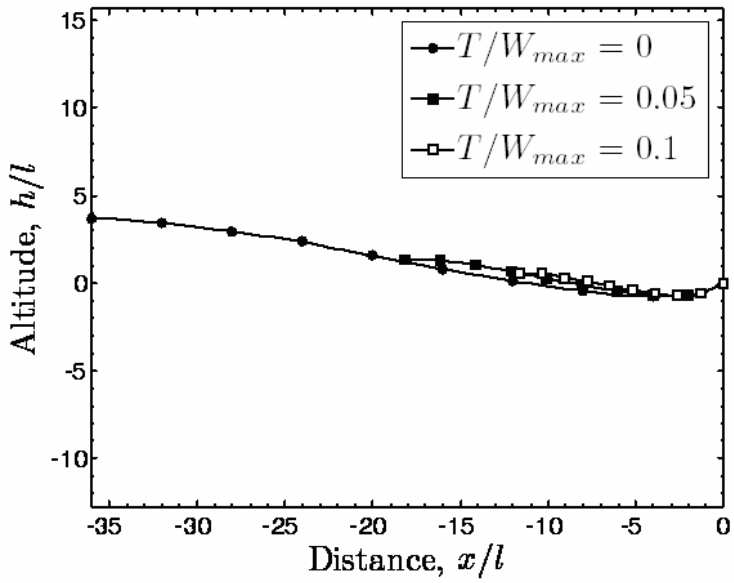

Figure 3.20: Full trajectories of varying maximum thrust-to-weight ratio for the aircraft with morphing

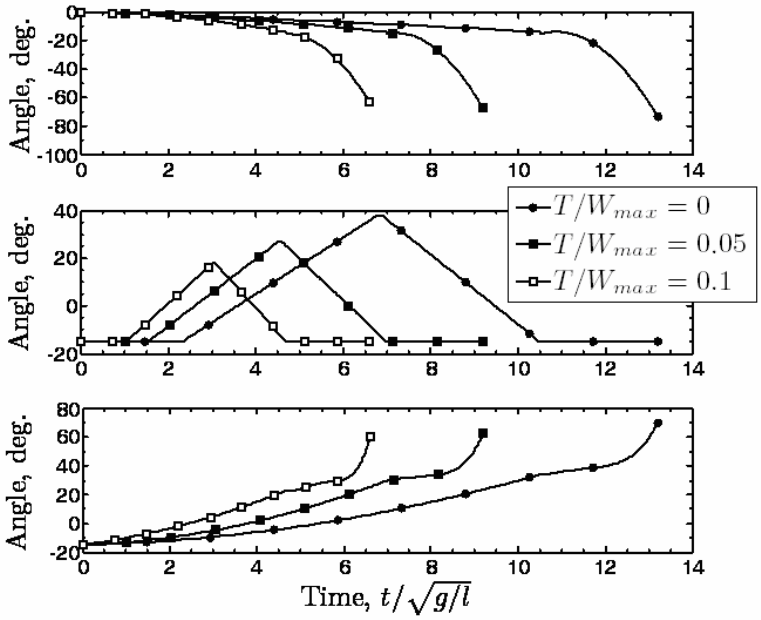

Figure 3.21 Climb phase morphing parameter time histories of varying maximum thrust-to-weight ratio: wing incidence (top), tail boom angle (middle), and tail incidence (bottom)

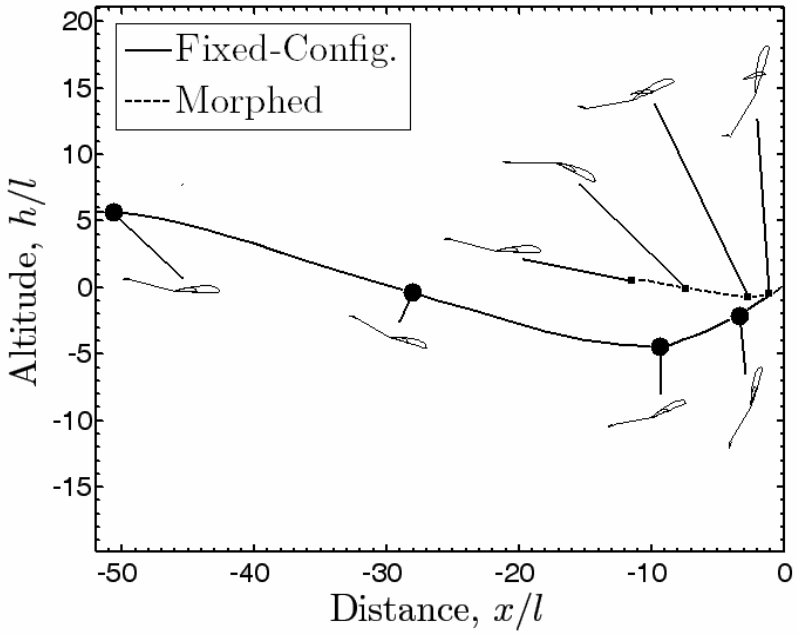

Figure 3.22: Comparison of fixed-configuration and morphing aircraft perching trajectories ($T/W_{max} = 0.1$)

Finally, the controllability of the aircraft during the perching maneuver is studied. Specifically, the effectiveness of the elevators is discussed, since the aircraft is only simulated in the longitudinal plane. Figure 3.23 depicts the maximum change in pitching moment coefficient from the nominal along the trajectory due to elevator deflection in the upwards and downwards directions. Thus, this plot represents the additional control authority, useful for disturbance rejection, for example, available throughout the maneuver. In Figure 3.23, the cases in which the maximum thrust-to-weight ratio is 0.1 and the center of gravity is located at the neutral point are compared between morphing and fixed-configuration aircraft. In general, the morphed case maintains high control authority in both directions throughout the maneuver. At the beginning and the end of the maneuver, the fixed-configuration case only has authority in one direction because the elevators are fully deflected in order to track the optimal trajectory. The morphed case is worse around 15% through the maneuver because the tail boom is briefly rotating the elevators into the stalled regime in order to pitch the aircraft downwards. This problem could be alleviated by factoring in controllability into the cost function. Indeed, this flexibility is one of the hallmarks of adding additional morphing degrees of freedom to the airframe.

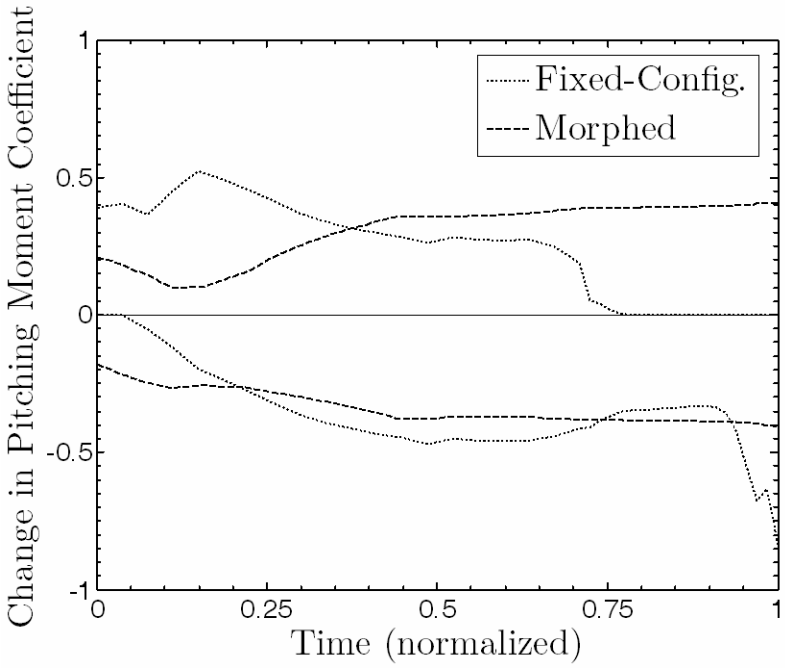

Figure 3.23: Elevator effectiveness for fixed-configuration and morphing aircraft

5. Conclusion

The problem of designing a trajectory to perch a low thrust-to-weight aircraft on a platform has been formulated and solved for a variety of cases: point-mass, conventional, and morphing airframes. It has been shown that the combination of low required landing speed and low thrust-to-weight ratio invariably leads to undershoot in the perching trajectory. If this undershoot is to be minimized, then the trajectory can be effectively broken into two sub-problems: the dive phase and the climb phase. Solving the point-mass aircraft dynamics produces a simpler trajectory optimization problem and provides an optimistic solution to the more complicated problem of conventional aircraft dynamics. These simulations have shown that the aircraft must pitch up to high angles of attack in order to produce enough drag to slow the aircraft over a reasonable distance. With pitch dynamics included, the location of the center

of gravity becomes a very important factor in determining the cost of the optimal trajectory. It has been demonstrated that pitch instability improves the perching trajectories in the sense of reducing their spatial bounds. Finally, the addition of a few judicious morphing degrees of freedom has been shown to improve the optimal perching trajectory and to increase the effectiveness of the control surfaces throughout the maneuver.

REFERENCES

[1] Sanders, B., Crowe, R., and Garcia, E., "Defense Advanced Research Projects Agency: Smart Materials and Structures Demonstration Program Overview," *Journal of Intelligent Material Systems and Structures*, Vol. 15, No. 4, 2004, 227–233.

[2] Bowman, J., Sanders, B., and Weisshaar, T., "Evaluating the Impact of Morphing Technologies on Aircraft Performance," AIAA2002-1631, 2002.

[3] Wickenheiser, A., Garcia, E., and Waszak, M., "Evaluation of Bio-Inspired Morphing Concepts with Regard to Aircraft Dynamics and Performance," *Proceedings of SPIE: International Society for Optical Engineering*, Vol. 5390, 2004, pp. 202–211.

[4] Tidwell, Z., Joshi, S., Crossley, W. A., and Ramakrishnan, S., "Comparison of Morphing Wing Strategies Based Upon Aircraft Performance Impacts," AIAA 2004-1722, 2004.

[5] Bye, D. R., and McClure, P. D. "Design of a Morphing Vehicle," AIAA-2007-1728, 2007.

[6] Flanagan, J. S., Strutzenberg, R. C., Myers, R. B., and Rodrian, J. E. "Development and Flight Testing of a Morphing Aircraft, the NextGen MFX-1," AIAA2007-1707, 2007.

[7] DeLaurier, J.D. "The Development and Testing of a Full-Scale Piloted Ornithopter," *Canadian Aeronautics and Space Journal*, Vol. 45, No. 2, 1999, pp. 72-82.

[8] Wickenheiser, A., Garcia, E., and Waszak, M., "Longitudinal Dynamics of a Perching Aircraft Concept," *Proceedings of SPIE: International Society for Optical Engineering*, Vol. 5764, 2005, pp. 192–202.

[9] Wickenheiser, A., and Garcia, E. "Longitudinal Dynamics of a Perching Aircraft," *Journal of Aircraft*, Vol. 43, No. 6, 2006, pp. 1386-1392.

[10] McGahan, J. "Gliding Flight of the Andean Condor in Nature," *Journal of Experimental Biology*, Vol. 58, 1973, pp. 225-237.

[11] Crowther, W. J., "Perched Landing and Takeoff for Fixed Wing UAVs," *NATO Symposium on Unmanned Vehicles for Aerial, Ground, and Naval Military Operations*, Ankara, Turkey, 2000.

[12] Levine, J. S., Blaney, D. L., Connerney, J. E. P., Greeley, R., Head, J. W., Hoffman, J. H., Jakosky, B. M., McKay, C. P., Sotin, C., and Summers, M. E., "Science from a Mars Airplane: The Aerial Regional-Scale Environmental Survey (ARES) of Mars," AIAA2003-6576, 2003.

[13] Enright, P. J., and Conway, B. A., "Discrete Approximations to Optimal Trajectories Using Direct Transcription and Nonlinear Programming," *Journal of Guidance, Control, and Dynamics*, Vol. 15, No. 4, 1992, pp. 994-1002.

[14] Fritsch, F. N., and Carlson, R. E., "Monotone Piecewise Cubic Interpolation," *SIAM Journal on Numerical Analysis*, Vol. 17, No. 2, 1980, pp. 238-246.

[15] Atiqullah, M. M., "Tuned Annealing for Optimization," *Lecture Notes in Computer Science*, Vol. 2074, 2001, pp. 669-679.

[16] Powell, M. J. D., "A Fast Algorithm for Nonlinearly Constrained Optimization Calculations," *Numerical Analysis*, edited by G. A. Watson, Lecture Notes in Mathematics, Springer Verlag, Vol. 630, 1978, pp. 144–157.

[17] Dormand, J. R., and Prince, P. J. "A family of embedded Runge-Kutta formulae," *Journal of Computational and Applied Mathematics*, Vol. 6, 1980, pp 19-26.

[18] Betts, J. T., *Practical Methods for Optimal Control Using Nonlinear Programming*, SIAM, Philadelphia, 2001, Chap. 1.

[19] Wickenheiser, A., and Garcia, E., "Perching Aerodynamics and Trajectory Optimization," *Proceedings of SPIE: International Society for Optical Engineering*, Vol. 6525, 2007, 65250O.

[20] Weissinger, J., "The Lift Distribution of Swept-Back Wings," NACA, TM-1120, 1947.

[21] Wickenheiser, A., and Garcia, E., "Aerodynamic Modeling of Morphing Wings Using an Extended Lifting-Line Analysis," *Journal of Aircraft*, Vol. 44, No. 1, 2007, pp. 10-16.

[22] Sheldahl, R. E., and Klimas, P. C., "Aerodynamic Characteristics of Seven Symmetrical Airfoil Sections Through 180-Degree Angle of Attack for Use in Aerodynamic Analysis of Vertical Axis Wind Turbines," Sandia National Laboratories Report, SAND80-2114, 1981.

[23] Goman, M., and Khrabrov, A., "State-Space Representation of Aerodynamic Characteristics of an Aircraft at High Angles of Attack," *Journal of Aircraft*, Vol. 31, No. 5, 1994, pp. 1109-1115.

This chapter originally appeared as:

Wickenheiser, A., and Garcia, E. "Optimization of Perching Maneuvers Through Vehicle Morphing," *Journal of Guidance, Control, and Dynamics*, (in review).